nature communications

Article

https://doi.org/10.1038/s41467-026-74972-3

Design, synthesis and structural mechanism of action of TRPV1 agonist MSP20 with long-lasting analgesic effect

Received: 20 June 2025

Accepted: 18 June 2026

Published online: 06 July 2026

Check for updates

Arthur Neuberger[1,12], Isabella Romeo[2,3,12], Francesca Aiello[4,12], Alexey Alekseev[1,12], Samuele Maramai[5] ✉, Federica Pessina[6], Chiara Vagaggini[5], Federica Poggialini[5], Elena Dreassi[5], Maria Frosini[7], Aniello Schiano Moriello[8,9], Luciano De Petrocellis[8], Andrea Maria Morace[10], Carmela Belardo[10], Michela Perrone[10], Roozbe Bonsale[10], Livio Luongo[10], Sabatino Maione[10], Irina A. Talyzina[1,11], Stefano Alcaro[2,3] ✉, Anna Artese[2,3,13], Antonella Brizzi[5,13] & Alexander I. Sobolevsky[1,13] ✉

Transient receptor potential vanilloid type-1 (TRPV1) channel is a polymodal receptor involved in pain perception and neuronal signalling that represents a promising target for the development of analgesics and neuroprotective agents. In this study we implement a combination of computational techniques and targeted design of chemical libraries to discover benzothiophene-substituted TRPV1 agonists with high affinity and efficacy toward TRPV1. In vitro functional experiments show that prolonged or repeated exposure to these compounds induce calcium-dependent desensitization of TRPV1, making it insensitive to noxious stimuli. We solve a cryo-electron microscopy (cryo-EM) structure of human TRPV1 (hTRPV1) in complex with the most promising benzothiophene-substituted agonist MSP20. The structure reveals molecular details of MSP20 binding to the vanilloid site and a desensitized conformation of hTRPV1, characterized by the closed ion channel pore, α-helical C-terminus and distinct behaviour of annular lipids. Our in vivo experiments demonstrate that MSP20 exhibits robust and long-lasting antinociceptive activity with ex-vivo neuroprotective effects, supporting the perspective of benzothiophene-substituted vanilloids as future analgesics.

The capsaicin receptor or transient receptor potential (TRP) vanilloid type-1 (TRPV1) channel is involved in the perception of noxious chemical, thermal, and mechanical stimuli[1]. Being a polymodal sensor, TRPV1 represents a nociceptive and temperature-sensitive TRP channel (thermo TRP). Consistent with its role in pain perception, TRPV1 is mainly expressed in central and peripheral capsaicin-sensitive neurons of the brain, spinal cord and sensory ganglia. TRPV1 is also expressed in non-neuronal cells, such as astrocytes, adipocytes, immune and muscle cells[2], indicating its involvement in numerous other physiological and pathophysiological processes. Activation of TRPV1 induces the release of various neuropeptides, which activate secondary spinal cord neurons and elicit biochemical cascades in the peripheral tissue that lead to neurogenic inflammation. Neurogenic inflammation can also occur in the central nervous system (CNS) in response to neuroinflammatory events in the brain or spinal cord[3]. Paradoxically, prolonged or repeated stimulation of TRPV1 induces its calcium-dependent desensitization, rendering the receptor insensitive to common agonists, such as capsaicin, and other noxious stimuli, as well as silencing the entire nerve terminal[4,5]. This phenomenon provides the basis for the topical use of capsaicin in the treatment of painful

A full list of affiliations appears at the end of the paper. ✉e-mail: samuele.maramai@unisi.it; alcaro@unicz.it; as4005@cumc.columbia.edu

neuropathic conditions[6] and paves the way for the development of analgesics endowed with long-lasting pain-relieving activity[7]. Moreover, since capsaicin reduces brain oxidative stress, neuroinflammation and neuronal cell death, TRPV1-targeting molecules may be useful for the treatment of various brain disorders[8,9].

Using in silico-guided rational drug design, we synthesized a class of TRPV1 agonists[10]. These compounds include fundamental structural elements for triggering ligand-channel interaction[11,12], namely a 4-(5-substituted-thien-2-yl)butanoyl moiety in place of the nonenoyl chain of capsaicin, an aromatic head bearing hydrogen bond donor/acceptor groups, and the amide residue as a linker. Lipophilic substituents, such as the iodine atom or a flat and freely rotating pyridine/benzene ring at position 5 of the thiophene nucleus, furnished several amides with high efficacy and affinity toward TRPV1 compared to capsaicin[10].

Here we present a useful strategy in drug discovery and development, combining computational techniques and targeted design of chemical libraries, which allows us to select lipophilic vanilloid compounds with improved efficacy and selectivity toward TRPV1. Based on the molecular docking and Molecular Mechanics - Generalized Born Surface Area (MM-GBSA)[13] energy estimation to simulate and predictively refine the ligand-target interactions, we introduce benzothiophene as a lipophilic structural component of the TRPV1 ligands. Benzothiophene promotes hydrophobic interactions of agonists with aromatic residues in the active site as well as improves affinity and permeability of these compounds across the biological membranes. We synthesize a series of 3-(benzo[*b*]thiophen-2-yl)propancarboxamides characterized by either the vanillyl moiety of capsaicin or by aromatic amines with or without hydrogen bond donor/acceptor groups in the para/meta-positions in the amidic portion. Our in vitro functional experiments demonstrate that the synthesized benzothiophene-substituted agonists induce calcium-dependent desensitization of TRPV1, while our in vivo experiments confirm the improved analgesic properties of the most promising compound **6**, MSP20, compared to 4-(5-substituted-thiophen-2-yl)butanamides, without inducing thermoregulatory side effects. Likewise, we assess the in vitro absorption, distribution, metabolism, and excretion (ADME) properties of MSP20 and its safety profile. Since MSP20 displays reasonable physicochemical characteristics for crossing the blood brain barrier (BBB), its potential neuroprotective activity is investigated in rat brain slices, revealing significant TRPV1-mediated neuroprotective effects. To highlight the molecular mechanism of antinociceptive and potential neuroprotective activity, we solve a cryo-EM structure of human TRPV1 (hTRPV1) in complex with MSP20, confirming binding of this compound to the vanilloid site, one of the most common among numerous regulatory sites identified in TRP channels[14,15]. In addition, our structural analysis demonstrates that MSP20 converts hTRPV1 into the desensitized state, thus providing a template for the development of the next generation analgesics capable of offering long-lasting pain relief and potential neuroprotection.

Results and discussion

Rational drug design

Recent structures of hTRPV1 in the apo state or in complex with potent analgesics[16] have provided a template for exploring the vanilloid binding pocket. As a first step, we analysed the binding modes of the most promising compounds from our previous study to guide rational modifications[10]. Molecular docking revealed that compound **2a** binds to the vanilloid site in a manner similar to capsaicin, forming a π-π interaction with Y511 and a hydrogen bond with E570 via its hydroxyl group, while its carbamoyl oxygen also interacts with Y511. In contrast, compound **3a** reorients its hydroxyl group to establish a hydrogen bond with N551, thereby losing the π-π interaction (Supplementary Fig. 1). Since **2a** exhibited higher affinity towards TRPV1, whereas **3a** demonstrated superior in vivo efficacy, our next challenge was to refine the lead compound to balance the activity and physicochemical properties[10]. The lack of interactions in the tail portion highlighted it as a key region for further optimization. We therefore designed a library of derivatives based on the **2a**-TRPV1 complex[10], aiming to enhance binding interactions and optimize pharmacological potential. Using Ligand Designer, we systematically modified the ligand to increase its binding affinity. In particular, 122 ring systems, including five- and six-membered rings as well as fused heterocycles, were introduced to replace key regions of the ligand (tail). Additionally, a linker containing 1 to 3 methylene units was incorporated to evaluate the impact on flexibility between the lipophilic moiety and the vanilloid portion. The resulting 366 structures underwent comprehensive computational and visual analysis to assess their drug-likeness. Prior to docking, pharmacologically relevant properties were evaluated to filter out unsuitable ligands and exclude those containing reactive groups. Molecules with chiral centres or violations of Lipinski's Rule of Five or Rule of Three were discarded. Only compounds predicted to show a qualitative CNS activity[17] were retained, specifically those with a CNS parameter >−1[18]. Furthermore, five compounds containing imine groups, which may undergo hydrolysis, were removed from the dataset. This rigorous filtering process ensured that only the most promising candidates in terms of ADME properties advanced to the docking stage and further optimization.

The refined library was then docked to the cryo-EM structure of hTRPV1 in complex with SB-366791 (PDB: 8GFA)[16] using the Glide method (Schrödinger Release 2020-4: Glide, Schrödinger, LLC, New York, NY) with the standard precision (SP) protocol, centring the grid box on the bound ligand. To validate the docking protocol, we compared the root mean square deviation (RMSD) values between the experimental ligand pose and those generated by docking calculations, achieving an RMSD of 0.4 Å and a Glide GScore of −9.45 kcal/mol and thus confirming the accuracy of our approach. Glide GScore values for the screened compounds ranged from −6.6 to −10.2 kcal/mol. A subset of 28 ligands with better scores compared to the re-docking threshold was selected for further refinement and subjected to MM/GBSA thermodynamic analysis, including SB-366791 as a reference compound (ΔG_{bind} = −91.42 kcal/mol). Three ligands showed superior binding affinity and were assessed for synthetic accessibility (Supplementary Table 1); the benzo[*b*]thiophene derivative was prioritized due to its straightforward synthesis and the commercial availability of its starting acid (Fig. 1).

Chemistry and in vitro calcium uptake measurements

The synthetic procedure leading to compounds **2**–**9** was relatively straightforward, as depicted in Table 1. Indeed, a series of selected aromatic amines was condensed with 3-(benzo[*b*]thiophen-2-yl)propanoic acid **1**, using two different condensing systems, i.e., *O*-(benzotriazol-1-yl)-*N*,*N*,*N*′,*N*′-tetramethyluronium hexafluorophosphate/1-hydroxybenzotriazole (HBTU/HOBt) and *N*,*N*-diisopropylethylamine (DIPEA) as the base in dry *N*,*N*-dimethylformamide (DMF), method A, or *N*-(3-Dimethylaminopropyl)-*N*′-ethylcarbodiimide (EDC)/HOBt, in dry dichloromethane (DCM) or acetonitrile (ACN), method B, when the acid was coupled with the hydrochloride salt of the amine or with the free amine, respectively. Amide **5** was also obtained by demethylation reaction on the crude amide **4** using BBr_3 in refluxing dry toluene in moderate yield. Title compounds **2**–**9** were obtained with acceptable to high yields as cream or white solids after chromatographic purification.

Functional effects of all final amides **2**–**9** on human recombinant TRPV1 stably overexpressed in human embryonic kidney (HEK 293) cells were evaluated using the Fluo-4-AM-based fluorescent measurements of intracellular calcium. To assess the selectivity of the most interesting derivatives, **2** and **6**, the same in vitro assay was also applied to rat TRPA1 (rTRPA1), which represents another principal transducer

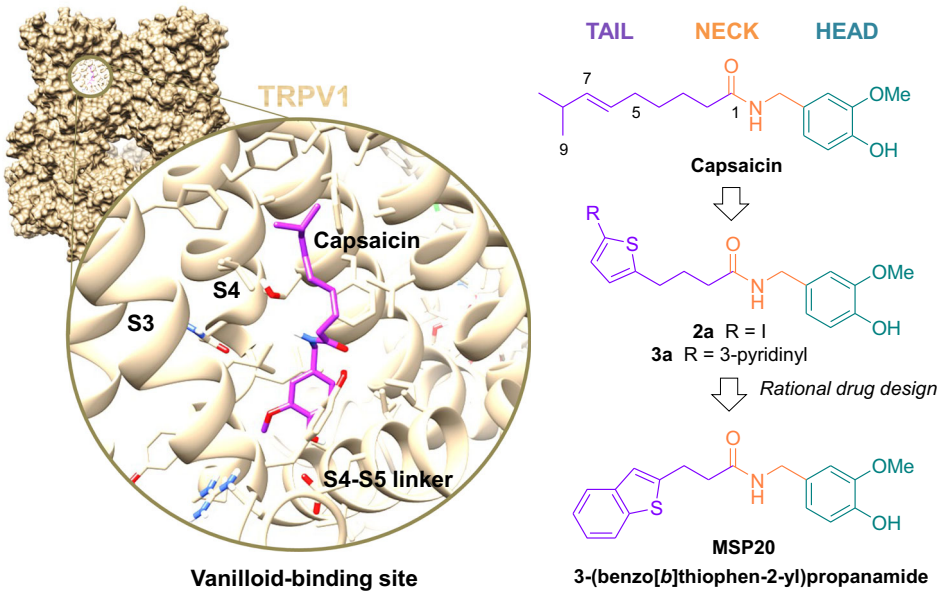

Fig. 1 | Chemical design. Chemical features of capsaicin and 2D structures of synthesized amide derivatives, designed through a rational drug design approach targeting the vanilloid-binding site of TRPV1.

of painful stimuli[19]. Both hTRPV1 and rTRPA1 were activated by natural agonists, capsaicin and allyl isothiocyanate (AITC), respectively. Changes in intracellular calcium concentration ($[Ca^{2+}]_i$) were used as a measure of compound-induced activation (EC_{50}, the concentration of the test compound exerting a half-maximal agonist effect) or inhibition/desensitization (IC_{50}, the concentration exerting a half-maximal inhibition of agonist-induced $[Ca^{2+}]_i$ elevation determined by measuring the reduction of signal induced by 0.1 μM capsaicin for TRPV1 or 100 μM AITC for TRPA1 after 5-min preincubation of cells with the test compound). For the efficacy at TRPV1 and TRPA1, percent values were normalized to the maximum value of Ca^{2+} influx measured in response to application of 4 μM ionomycin or 100 μM AITC, respectively (Supplementary Fig. 2). The results of calcium uptake measurements are summarized in Table 1.

The analysis of the functional assay results confirmed the validity of introducing the 3-(benzo[*b*]thiophen-2-yl)propanoyl moiety in place of the nonenoyl chain of capsaicin since all synthesized compounds were able to activate TRPV1. Compounds **2, 5, 6**, and **8** showed efficacy values equal or higher than 50% and, in particular, derivatives **6** and **8**, although less potent, behaved as strong TRPV1 agonists endowed with efficacy similar to that of capsaicin. The most active compounds share a phenol moiety, although placed at different distance from the amide functionality (see compounds **2, 5, 6**, and **8**). The natural substitution pattern, the vanillyl moiety, was still optimal for TRPV1 activity providing the most effective and potent derivative **6** (MSP20, efficacy 78.24%, EC_{50} 46 nM). Moreover, both compounds **2** and **6**, i.e., MSP20, were unable to interact with the TRPA1 channel. To further test selectivity of the most interesting compound MSP20, we tested its functional effects on rat recombinant TRPV3, TRPV4 and TRPM8 receptors, stably overexpressed in human embryonic kidney (HEK-293) cells. Similarly to experiments with TRPV1 and TRPA1, we estimated MSP20 activating potency by measuring EC_{50} (normalized to the maximum Ca^{2+} influx effect on intracellular Ca^{2+} concentration observed with application of 4 μM ionomycin) or inhibitory/desensitizing potency by measuring IC_{50} (determined against the effect of agonists, 100 μM thymol for TRPV3, 10 nM GSK1016790A for TRPV4, or 0.25 μM icilin for TRPM8, after a 5-min preincubation with test compound). Remarkably, MSP20 appeared to be selective for TRPV1 (Supplementary Table 2).

Viability and cytotoxicity assay

To establish the biological profile of the most interesting TRPV1 agonist MSP20, its cytotoxicity and cell viability were evaluated either on HaCaT (keratinocytes) or on HUVEC (endothelial) cell line, before proceeding to ex vivo (brain slices) or in vivo (mice) studies. HaCaT and HUVEC cells were treated with the increasing (0.1–10 μM) concentrations of MSP20 for 24 and 48 hours. The results indicated that MSP20 did not modify lactate dehydrogenase (LDH) release (Supplementary Fig. 3A–D) and did not induce significant cytotoxicity in both cell lines at concentrations up to 10 μM (Supplementary Fig. 3E–H) ($p > 0.05$), proving to be well tolerated by HaCaT and HUVEC cells.

Protective role of MSP20 against ROS production induced by glucose oxidase exposure in keratinocytes and endothelial cells

To evaluate a possible antioxidant effect of MSP20, the production of reactive oxygen species (ROS) was measured both in HaCaT and HUVEC cells exposed to glucose oxidase (GO) and treated with MSP20 at different concentrations (0.1–100 μM).

As shown in Fig. 2, MSP20 induced a reduction in ROS production in both cell lines following a U-shaped concentration–response relationship. At concentrations of 0.1, 10, and 100 μM, MSP20 significantly decreased ROS fluorescence intensity ($P < 0.001$), whereas the 1 μM concentration had no effect. These findings support the hypothesis that MSP20, by counteracting GO-induced oxidative damage, may help preserve redox homeostasis in keratinocytes and endothelial cells, especially at concentrations where its effect is most pronounced.

In vitro absorption, distribution, metabolism, and excretion (ADME) studies of MSP20

MSP20 is characterized by an acceptable thermodynamic aqueous solubility (5.68 ± 0.46 μg/mL, LogS −4.79), which is also confirmed by the apparent permeability (P_{app}) estimated using phosphatidylcholine and brain polar lipids to mimic the gastrointestinal barrier (1.27 ± 0.02) and BBB (0.66 ± 0.03). P_{app} values in both systems showed that MSP20 is characterized by low passive permeability, although more pronounced for BBB, with a low membrane retention % (MR%), suggesting that this compound is not particularly capable of interacting with the phospholipidic bilayer, in agreement with the aqueous solubility data (Supplementary Table 3). Furthermore, MSP20 exhibited excellent metabolic stability, greater than 95%, in the presence of Human Liver

https://doi.org/10.1038/s41467-026-74972-3

Table 1 | Synthetic procedure leading to 3-(benzo[*b*]thiophen-2-yl)propanamides 2–9

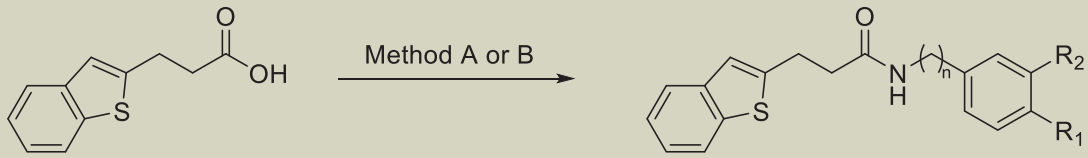

2-9

Nr	*n*	R^1	R^2	TRPV1 Eff. %	TRPV1 EC_{50} (μM)	TRPV1 IC_{50} (μM)	TRPA1 Eff. %	TRPA1 EC_{50} (μM)	TRPA1 IC_{50} (μM)
2	0	-OH	-H	70.4 ± 0.6	0.126 ± 0.006	0.35 ± 0.04	<10	n.a.	>100
3	1	-H	-H	34.5 ± 0.1	4.9 ± 0.1	>50	n.t.	n.t.	n.t.
4	1	$-OCH_3$	-H	17.28 ± 0.72	8.42 ± 1.17	>25	n.t.	n.t.	n.t.
5	1	-OH	-H	50.00 ± 0.52	2.45 ± 0.13	6.2 ± 0.3	n.t.	n.t.	n.t.
6 MSP20	1	-OH	$-OCH_3$	78.24 ± 1.77	0.046 ± 0.008	0.044 ± 0.008	<10	n.a.	>100
7	1	-Cl	-Cl	31.90 ± 0.57	7.92 ± 0.90	5.4 ± 0.9	n.t.	n.t.	n.t.
8	2	-OH	-OH	78.5 ± 0.4	0.53 ± 0.01	0.53 ± 0.06	n.t.	n.t.	n.t.
9	2	$-OCH_3$	-Cl	33.1 ± 0.4	9.0 ± 0.2	14.8 ± 4.0	n.t.	n.t.	n.t.
capsaicin				78.6 ± 0.6	0.0053 ± 0.0004	0.0080 ± 0.0003	-	-	-
AITC				-	-	-	65.9 ± 0.5*	1.41 ± 0.04	1.71 ± 0.06

Method A: suitable amine hydrochloride, HBTU, HOBt, DIPEA, dry DMF, rt, 12 h (**6** and **8**); Method B: suitable substituted amine or aniline, EDCI, HOBt, dry DCM (**3**, **4**, **7**, and **9**) or HPLC grade ACN (**2** and **5**), rt, 12 h; Data are means ± SEM, *N* = 3; TRPV1 Eff. % determined as percent of 4 μM ionomycin; TRPV1 IC_{50} determined against the effect of capsaicin 0.1 μM; TRPA1 Eff. % determined as percent of 100 μM AITC; TRPA1 IC_{50} determined against the effect of 100 μM AITC; *n.a.* not active, *n.t.* not tested. *TRPA1 Eff. % determined as per cent of 4 μM ionomycin. Source data are provided as a source data file.

https://doi.org/10.1038/s41467-026-74972-3

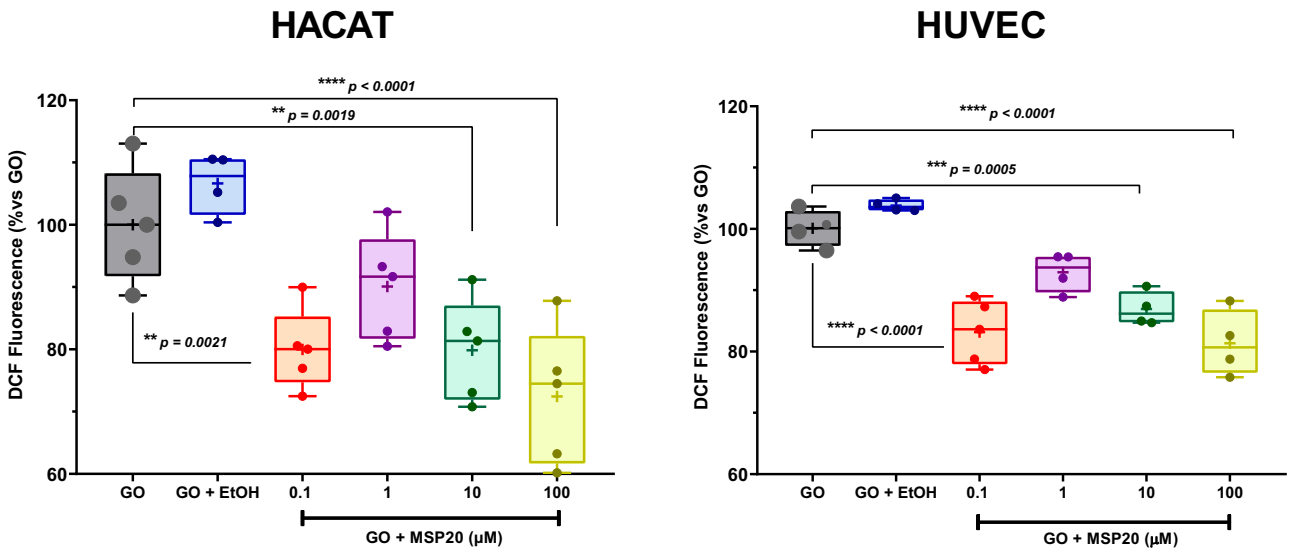

Fig. 2 | Protective effect of MSP20 on oxidative stress-induced damage of HaCaT and HUVEC cells. Cells were pretreated with MSP20 (0.1–100 µM) for 24 hours and then exposed to GO for 30 minutes. ROS were detected using the DCFH-DA fluorescence assay (485 nm excitation/530 nm emission). Data are mean ± SEM (biological replicates HaCaT $n = 5$, HUVEC $n = 4$; technical replicates 4–5) and reported as a percentage value of GO, taken as 100%. Whiskers between min to max; horizontal line median; + mean value; dots single points. Statistical analysis: GO vs MSP20, one-way ANOVA and Bonferroni multiple comparisons test. Source data are provided as a source data file.

Microsomes (HLMs) with a minimal metabolite formation (4.17%) which could result from oxidation at the benzothiophene ring (Supplementary Fig. 4). The value of plasma stability obtained for this compound was higher than 91% after 24 h of incubation, in line with its remarkably high half-life, highlighting once again the excellent stability of MSP20 in biological matrices. The high in vitro stability values indicate low susceptibility to microsomal metabolism and plasma esterases, giving us a preliminary idea of how the compound might behave in in vivo studies, where its exposure to more complex systems could be influenced by additional pharmacokinetic factors, including distribution, protein binding, and transporter-mediated clearance.

Neuroprotective activity of MSP20 in ex vivo assay

Modulation of TRPV1 can exert protective effects, particularly against excitotoxic damage, by regulating calcium influx, reducing excessive neuronal excitability, and mitigating the inflammatory responses, thereby preserving cellular viability and function under neurotoxic conditions[8]. The neuroprotective effects of MSP20 have been evaluated in rat brain slices, an ex vivo powerful model to study neuroprotection as it preserves the complex architecture and functional connectivity of neuronal circuits while allowing precise experimental manipulation. Brain slices were exposed to glutamate (GLU) to induce excitotoxic injury. This well-established paradigm of neuronal damage, extensively validated in both cellular[20,21] and slice-based systems[22–25], was selected because it recapitulates key pathological features observed in stroke[26], traumatic brain injury[27], and neurodegenerative disorders[28]. Exposure of the brain slices to GLU led to the significant reduction in mitochondrial metabolic activity (slices viability) compared to control ($P < 0.001$), confirming the cytotoxic effects of GLU. In the presence of MSP20 and GLU, we observed a neuroprotective effect of MSP20, as demonstrated by a significant recovery of mitochondrial function compared to GLU treatment alone ($P < 0.01$). The observed MSP20-mediated protection, however, should be interpreted as a global tissue-level effect, as the present data do not allow discrimination between neuronal, glial, or neuron–glia interaction–dependent contributions. Moreover, the MSP20-mediated effect followed a U-shaped curve, characterized by a neuroprotective window of 10 nM–100 nM (Supplementary Fig. 5).

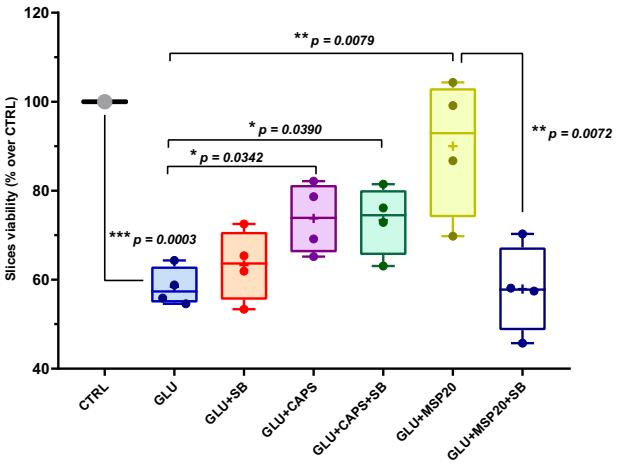

Fig. 3 | Effect of TRPV1 modulation on rat brain slice viability in the model of glutamate-induced excitotoxicity. Slice viability is plotted as a percentage relative to the control (CTRL) condition, taken as 100%. CTRL, untreated control slices. GLU, slices exposed to glutamate 60 mM to induce excitotoxic damage. TRPV1 ligands were used at the following concentrations: 10 µM of antagonist SB-366791 (SB), 0.1 µM of agonist capsaicin (CAPS) and 0.1 µM of agonist MSP20. Data are mean ± SEM, $n = 4$ of biological replicates (3–6 technical replicates/experiment). Whiskers between min to max; horizontal line median; + mean value; dots single points. Statistical analysis: CTRL vs GLU, one sample t test, two-tailed. Others: one-way ANOVA and Bonferroni multiple comparisons test. Source data are provided as a source data file.

To further investigate the mechanism underlying the neuroprotective effects of MSP20, we used the potent and selective TRPV1 receptor antagonist SB-366791[16], and compared the effects of MSP20 and SB-366791 to those of capsaicin (CAPS, Fig. 3). In GLU-treated slices, CAPS exerted a significant neuroprotective effect that was not reversed when SB-366791 was co-applied with CAPS, demonstrating that TRPV1 activation is not fully required for the observed neuroprotection. On the other hand, MSP20 significantly improved slice

viability in GLU-treated slices, and this effect, being even greater than that of capsaicin, was completely reversed by SB-366791 (Fig. 3), confirming the involvement of TRPV1 in MSP20-mediated neuroprotection. The persistence of CAPS-mediated neuroprotection despite TRPV1 antagonism may appear unexpected. However, previous studies showed that in different cellular contexts and experimental models, CAPS can act through both TRPV1-dependent and -independent pathways[8]. Acting through these non-canonical mechanisms, CAPS was reported to protect AF5 mesencephalic cells from NMDA-induced toxicity[29], enhance memory and synaptic plasticity in Alzheimer's disease models[30], and exert anti-inflammatory effects in Parkinson's disease models[8]. In addition, it suppresses iNOS and COX-2 expression in macrophages via NF-κB and AP-1 inhibition[31], further supporting TRPV1-independent signalling.

Moreover, CAPS exhibits robust antioxidant activity in DPPH and ABTS assays (Supplementary Table 4), comparable to Trolox, whereas MSP20, although active, shows lower potency on a molar basis. These findings suggest that CAPS may provide neuroprotection partly through its strong free radical-scavenging capacity[32–34], while MSP20 requires higher concentrations to achieve comparable antioxidant effects. On the other hand, MSP20 protects brain slices from glutamate-induced injury at 0.1 μM, a concentration that is devoid of antioxidant activity (ABTS and DPPH assays) or shows only minimal activity in GO cell-based assays, suggesting that the neuroprotective effects are likely independent from antioxidant mechanisms.

Taken together, these data indicate that TRPV1 activation confers protection against excitotoxic damage in rat brain slices. The neuroprotection induced by TRPV1 agonists (MSP20 and CAPS) and its reversal by TRPV1 antagonism (SB-366791) support a beneficial role of TRPV1 signalling under excitotoxic conditions in this ex-vivo model. Notably, CAPS appears to act through multiple mechanisms, including TRPV1-independent antioxidant pathways, whereas MSP20-mediated neuroprotection seems to be strictly dependent on the canonical TRPV1 ion channel activation.

In vivo antinociceptive activity of MP20 in mice

Considering the results obtained in the in vitro and ex vivo assays, we investigated the potential antinociceptive effect of the most interesting derivative, compound MSP20, in vivo by studying the formalin-induced nocifensive behaviour in mice. Mice received the subcutaneous injection of vehicle (veh) in the dorsal surface of the hind paw followed by formalin (Form, 1.25%, 30 μL) injection 10 min later. Noxious behaviour was observed immediately after the formalin injection and lasted for 0–10 min. The nocifensive behaviour was characterized by the first phase that lasted 2.45 ± 0.11 min. The first phase was followed by the second phase of nocifensive behaviour, reflecting the development of nociceptive sensitization in the dorsal horn of the spinal cord[35,36]. The nocifensive behaviour in the second phase started 30 min after the formalin administration and lasted for 1.66 ± 0.06 min. Subcutaneous administration of the highest and particularly the intermediate doses of MSP20 into the hind paw (0.015 μg/paw and 0.15 μg/paw) significantly reduced the nocifensive behaviour in the second phase (to 0.66 ± 0.25 min and 0.46 ± 0.11 min, respectively) compared to mice treated with vehicle (1.66 ± 0.06 min). The lowest dose (0.0075 μg/paw) did not show a pronounced significant effect (1.61 ± 0.18 min) in the second phase of the formalin test compared to mice treated with the vehicle. Interestingly, co-administration of the intermediate dose of MSP20 with IRTX, a TRPV1 antagonist, abolished its anti-nocifensive effect (1.13 ± 0.06 min) ($F_{(7.163, 322.3)} = 71.60$ time; $F_{(4,45)} = 16.85$ treatment; $F_{(48,540)} = 6.802$ time x treatment) (Fig. 4).

The results of the formalin test indicate that MSP20 exerts a significant antinocifensive effect, markedly at the intermediate doses. This suggests a non-linear, bell-shaped dose-response relationship, a phenomenon observed with several TRPV1-targeting compounds[10,12,37–39] and in agreement with neuroprotection experiments in brain slices. A plausible explanation for this effect is the dual role of TRPV1 in pain modulation. At intermediate doses, MSP20 may preferentially desensitize TRPV1 channels, reducing the nociceptive transmission and exerting analgesic effects. The lowest dose is possibly not able to sufficiently desensitize the channel, whereas the highest dose could have a pleiotropic effect on other unidentified targets. In conclusion, the bell-shaped dose-response curve observed for MSP20 likely reflects the complex pharmacodynamics of TRPV1 modulation. These findings highlight the importance of dose optimization in the development of TRPV1-targeting analgesics to maximize efficacy while minimizing the unintended pronociceptive effects.

Evaluation of the thermoregulatory effect of MSP20 in mice

To further characterize the physiological effects of MSP20, we evaluated its impact on body temperature regulation following subcutaneous administration by using a rectal thermocouple probe[40]. No significant changes between the CTRL/Vehicle and CTRL/MSP20 treated group were observed at all time points (pre-treatment and 30, 60, 90, 120 and 150 minutes following the injection) indicating that the compound does not interfere with thermoregulation homeostasis (Supplementary Fig. 6A). To further characterize the long-term profile of the compound under repeated administration, we measured body temperature at days 1, 3, and 7. Again, no changes in body temperature were observed in animals at any time point (Supplementary Fig. 6B).

MSP20 reduces tactile allodynia in a spared nerve injury (SNI) neuropathic pain model

To further validate the analgesic properties of MSP20, we employed the spared nerve injury (SNI) model of peripheral neuropathic pain[41]. The results of Von Frey test performed post SNI induction show that the mechanical threshold in SNI/Vehicle group decreased as compared to the CTRL/Vehicle group throughout the duration of the experiment ($P < 0.0001$). MSP20 subcutaneous repeated administration (7 days starting from the day of the surgery) significantly reduced the tactile allodynia (SNI/MSP20: 0.959 ± 0.318, $P = 0.0045$, as compared to SNI/Vehicle group: 0.095 ± 0.054). Interestingly, the MSP20 antiallodynic effect was still detectable after stopping treatment (7 days after injury) on both day 9 (SNI/MSP20: 0.763 ± 0.251, $P = 0.0305$ vs SNI/Vehicle: 0.095 g ± 0.052) and day 12 (SNI/MSP20: 0.959 ± 0.318, $P = 0.0045$ vs SNI/Vehicle: 0.095 g ± 0.054) ($F_{(4,28)} = 21.11$ x time, $F_{(2,14)} = 16.34$ x treatment, $F_{(8,41)} = 5.610$ time x treatment), while the effect was lost at day 14 (Fig. 5).

As shown in Fig. 5, animals subjected to spared nerve injury (SNI) exhibited a significant reduction in paw withdrawal thresholds compared to the CTRL/Vehicle group throughout the observation period, confirming the development of tactile allodynia. Treatment with MSP20, continued until day 7 post-SNI, significantly attenuated SNI-induced allodynia on days 7, 9, and 12 post-injury. Following the discontinuation of MSP20, its analgesic effect, still detectable at day 9 and 12, diminished, and paw withdrawal thresholds returned to levels comparable to the SNI/vehicle group by day 14. This indicates that the effect of MSP20 was treatment-dependent and reversible. These findings demonstrate that MSP20 effectively alleviates mechanical hypersensitivity in the SNI model. This action is consistent with TRPV1-mediated desensitization mechanisms reported in other pain paradigms.

Taken together, these findings suggest that MSP20 exerts its antinociceptive and antiallodynic effects without inducing thermoregulatory side effects, supporting its favourable safety profile as a TRPV1 agonist.

Structure of hTRPV1 in complex with compound MSP20

We purified hTRPV1 in micelles of glyco-diosgenin (GDN) (see Methods), supplemented it with 200 μM MSP20 and subjected it to single-

https://doi.org/10.1038/s41467-026-74972-3

A

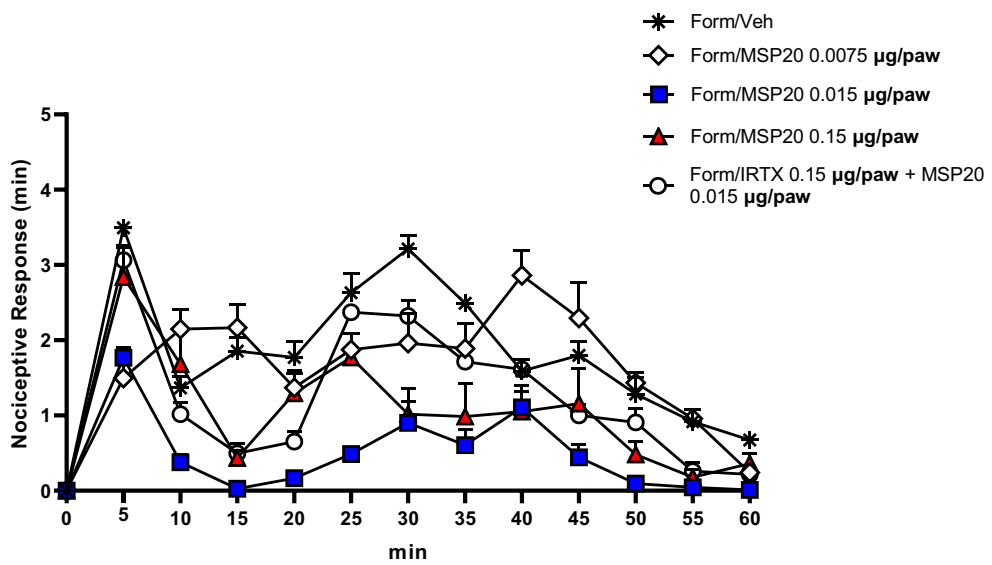

B

Group $*_{VS}$ *Form/veh*	*Acute phase*				*++Tonic phase*							
minutes	5	10	15	20	25	30	35	40	45	50	55	60
Form/ MSP20-**0.0075 µg/paw**	P <0,0001	P =0,0683	P =0,8047	P =0,4238	P =0,1076	P <0,0388	P =0,3061	P =0,0157	P =0,7358	P =0,9400	P =0,9971	P =0,0146
Form/MSP20 **0.015 µg/paw**	P <0,0001	P =0,0003	P <0,0001	P <0,0001	P <0,0001	P <0,0001	P <0,0001	P =0,2341	P =0,0002	P =0,0013	P =0,0014	P =0,0009
Form/MSP20 **0.15 µg/paw**	P =0,3959	P =0,9257	P <0,0001	P =0,5085	P =0,1442	P =0,0002	P =0,0266	P =0,4503	P =0,5347	P =0,0334	P =0,0056	P =0,2560
Form/**IRTX 0.15 µg/paw MSP20 0.015 µg/paw**	P =0,1085	P =0,3575	P <0,0001	P =0,0012	P =0,7257	P =0,0152	P =0,0125	P =0,9998	P =0,0144	P =0,5079	P =0,0141	P =0,0255

Fig. 4 | In vivo antinociceptive activity of MSP20 in mice. A Effect of vehicle (5% DMSO in 0.9% saline) or different doses of MSP20 (0.0075 µg/paw, 0.015 µg/paw, 0.15 µg/paw, 30 µL) and the co-administration with IRTX (0.15 µg/paw) administered on the dorsal surface of the hind paw 10 min before formalin (Form, 1.25%, 30 µL) on the nocifensive response expressed in min. **B** Table showing the statistical significance of the comparisons illustrated in the graph. Each time point represents the mean ± SEM of 10 mice per group. Two-way ANOVA followed by Dunnett's post hoc test. Effect estimates are presented with 95% confidence intervals (CI). Source data are provided as a source data file.

particle cryo-EM. Data processing revealed a single class of particles (Supplementary Fig. 7), which yielded a 2.6-Å resolution 4-fold-symmetrical 3D reconstruction (Fig. 6a, Supplementary Fig. 8, Supplementary Table 6) with clearly resolved density for the protein, annular lipids and four molecules of MSP20, one per hTRPV1 subunit (Supplementary Fig. 9). We built a molecular model of $hTRPV1_{MSP20}$, that includes an intracellular skirt mainly assembled of ankyrin repeat domains (ARDs) connected by 3-stranded β-sheets and a transmembrane domain (TMD), typical for the vanilloid family of TRP channels (Fig. 6b). The TMD is contributed by six transmembrane helices (S1–S6) and a re-entrant pore loop (P-loop) from each hTRPV1 subunit. S5, P-loop and S6 represent pore domains that assemble into a cation-selective channel in the middle of the TMD, while helices S1 through S4 form S1-S4 or voltage-sensing-like domains (VSLDs) that reside on its periphery. Each one of four identical densities, one per subunit of hTRPV1 tetramer, with the shape of an MSP20 molecule (Fig. 6c), resides in the vanilloid binding site located in the TMD region that faces the cytoplasmic leaflet of the membrane, at the interface between S1–S4 and pore domains (Fig. 6d). The vanilloid site in TRPV1 is known to bind other agonists, like capsaicin and resiniferatoxin (RTX), competitive antagonists such as capsazepine and SB-366791, as well as phosphatidylinositol (PI) in the absence of ligands (apo state)[14,16,42–46].

Validation of MSP20 binding to the vanilloid site in hTRPV1 using patch-clamp recordings

To assess the functional properties of human TRPV1 in response to MSP20, we performed patch-clamp recordings with rapid solution exchange from HEK293T cells expressing wild-type (WT) TRPV1. Prolonged application of 100 µM MSP20 produced a typical TRPV1-mediated current, which after an initial fast increase underwent pronounced reduction due to apparent desensitization (Fig. 7a, $\tau_{des} = 3.5 \pm 0.8$ s, $N = 4$, mean ± s.d.). The conditions of this functional experiment were similar to those used for cryo-EM grid preparation and indicate that TRPV1 can adopt a desensitized conformation while bound to MSP20. We next examined the concentration dependence of TRPV1 steady-state currents evoked by MSP20 (Fig. 7b). The data were well fit by the Hill equation, yielding an apparent Hill coefficient of 2.7 ± 1.3, consistent with cooperative activation. The resulting EC_{50} value (2.5 ± 1.8 µM) was higher than the reported EC_{50} values for capsaicin measured in patch-clamp experiments with HEK293 cells[16,47], in agreement with our calcium-imaging measurements.

The difference between the EC_{50} values of MSP20 and capsaicin obtained with the calcium fluorescence assay and the patch-clamp method is thought to likely depend on the type of assay itself. Indeed, the ratio between the capsaicin and MSP20 values obtained with the two methodologies is very similar, with capsaicin being approximately

https://doi.org/10.1038/s41467-026-74972-3

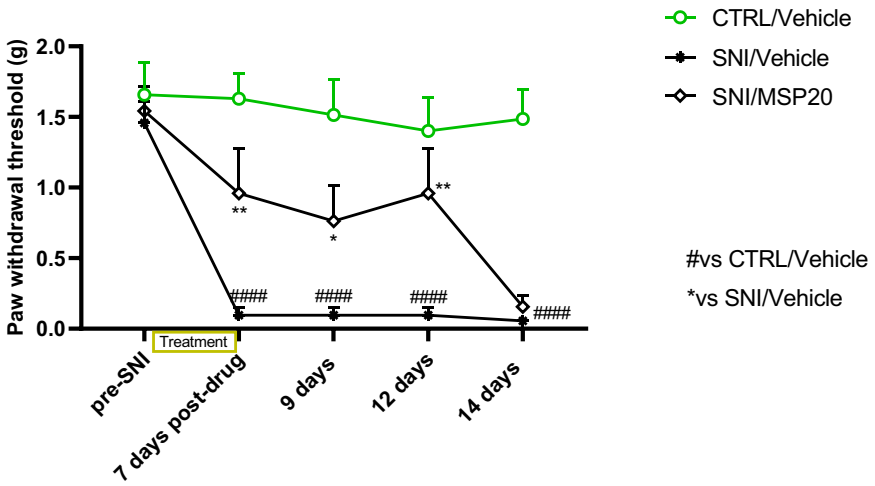

Fig. 5 | Effect of MSP20 on mechanical allodynia in the spared nerve injury (SNI) mouse model. Mice were subjected to spared nerve injury (SNI) to induce neuropathic pain and treated with MSP20 (7 mg/kg, subcutaneously) or vehicle (5% DMSO in 0.9% saline). Tactile allodynia was assessed using the Von Frey test at specified time points post-injury. Data are expressed as mean ± SEM with seven animals per group for each time-point of measurement. Inter-group differences were analysed using a two-way mixed-effects model (REML) for repeated measures, followed by Dunnett's multiple comparisons test. Spared nerve injury induced a mechanical hypersensitivity (from day 7 up to day 14: $p < 0.0001$, vs CTRL/Vehicle). MSP20 increased the paw withdrawal threshold from day 7 up to day 12 post-drug (day 7: $p = 0.0045$; day 9: $p = 0.0305$; day 12: $p = 0.0045$, vs SNI/Vehicle). $P < 0.05$ was considered statistically significant. $^{*}P < 0.05$. $^{**}P < 0.01$, vs SNI/Vehicle; $^{\#\#\#\#}P < 0.0001$ vs CTRL/vehicle. Effect estimates are presented with 95% confidence intervals (CI). Source data are provided as a source data file.

an order of magnitude more potent than MSP20. Consistent with this, the literature shows different EC_{50} values for capsaicin depending on the method used for calcium measurements[47–50].

To functionally interrogate the MSP20 binding pocket, we introduced the mutations Y511A, S512A, R557K, R557A, and A666W (Fig. 7c) and assessed their effects on MSP20-dependent activation. Mutations at R557 (R557K and R557A) as well as A666W abolished channel activation (Fig. 7d), consistent with a critical role for R557 in MSP20 coordination and suggesting that substitution of A666 with tryptophan introduces a steric clash that prevents MSP20 binding. In contrast, Y511A and S512A remained activatable by MSP20, with only modest changes in current amplitude, but exhibited altered kinetic properties (Fig. 7e, f). The Y511A mutant showed significantly slowed activation kinetics and accelerated deactivation kinetics, suggestive of reduced MSP20 binding stability. The S512A mutant displayed activation kinetics comparable to WT. However, its deactivation kinetics could not be adequately described by a single exponential, suggesting strong cooperativity effects.

Together, our electrophysiological experiments directly demonstrated MSP20-induced desensitization of human TRPV1, defined its apparent activation potency, and provided functional validation of the MSP20 binding pocket through mutational perturbation of channel kinetics.

Conformational state of $hTRPV1_{MSP20}$

To assess the conformational state of $hTRPV1_{MSP20}$, we measured the ion channel pore radius (Fig. 8a). The pore has two narrow constrictions, one at the selectivity filter, formed by the backbone carbonyl oxygens of G644, and the other at the gate region, formed by I680. While the selectivity filter constriction is typically permeable to water and ions, isoleucines I680 come much closer to the pore centre than in the open state and create a hydrophobic seal, which makes the pore non-conductive, similarly to the apo state (Fig. 8b). The closed conformation of the ion channel pore in the presence of bound agonist suggests that the $hTRPV1_{MSP20}$ structure represents a desensitized state. To further interrogate the identity of the $hTRPV1_{MSP20}$ gating state, we looked at the conformation of the C-terminus. Compared to the coiled conformation that characterizes the apo state, the C-terminus of $hTRPV1_{MSP20}$ adopts an α-helical conformation (Fig. 8c, d), typical for the open or desensitized states of TRPV3[51] and TRPV4[52]. We also looked at several key interactions that differ between TRPV1 gating states. Thus, MSP20 reaches deep into the vanilloid site of $hTRPV1_{MSP20}$, where its hydroxyl group interacts with R557 in S4 by pulling it up extracellularly (Fig. 8e). In this position, R557 is close to E570 in S5 and capable of forming a salt bridge with this glutamate. The same interaction occurs in the presence of other agonists, like RTX[53] (Fig. 8e), but in the apo and competitive antagonist-bound states, R557 and E570 reside too far to interact[16] (Fig. 8f). Interestingly, the open state of TRPV1 is also stabilized by the hydrogen bond between Q561 and R579, causing changes in Y565 and F582 side chain conformations and accompanied by disappearance of a lipid near F582 (Fig. 8e). In $hTRPV1_{MSP20}$, Q561 and R579 are too distal for strong interaction, causing less changes in the side chain conformations of Y565 and F582 and, as a result, the lipid adjacent to F582 retains a similar position as in the apo state (Fig. 8f). Our observations, therefore, confirm that the gating state of $hTRPV1_{MSP20}$ is different from the closed apo and open states, and has all features of the desensitized state.

Molecular insights into the $hTRPV1_{MSP20}$ pore conformation

The molecular dynamics (MD)-based solvent-accessible surface area (SASA) analysis of the key residues G644, acting as the selectivity filter, and I680, functioning as the activation gate across the four subunits, revealed that $hTRPV1_{MSP20}$ exhibits a lower SASA compared to the open-state conformation (Fig. 9a–c). Specifically, the average SASA for GS44 is lower in $hTRPV1_{MSP20}$ compared to $TRPV1_{7RQW}$ structure. Among independent simulated replicates, the mean ± SD is 103.87 ± 9.59 Å² for $hTRPV1_{MSP20}$ and 128.55 ± 9.41 Å² for $TRPV1_{7RQW}$ ($n = 3$). The mean difference is -24.7 Å². Similarly, the average SASA for I680 exhibits a significantly lower value in $hTRPV1_{MSP20}$ (109.06 ± 3.01 Å²) compared to the open system (166.21 ± 4.81 Å²), with a mean difference of approximately 57.2 Å². This narrowing suggests a decreased surface exposure of these critical regions, potentially affecting water and ion permeation. Furthermore, an in-depth assessment of key intrapore distances evaluated dynamically corroborated these experimental findings. In particular, residues Q561 and R579 are farther apart in $hTRPV1_{MSP20}$ than in the open conformation, due to

https://doi.org/10.1038/s41467-026-74972-3

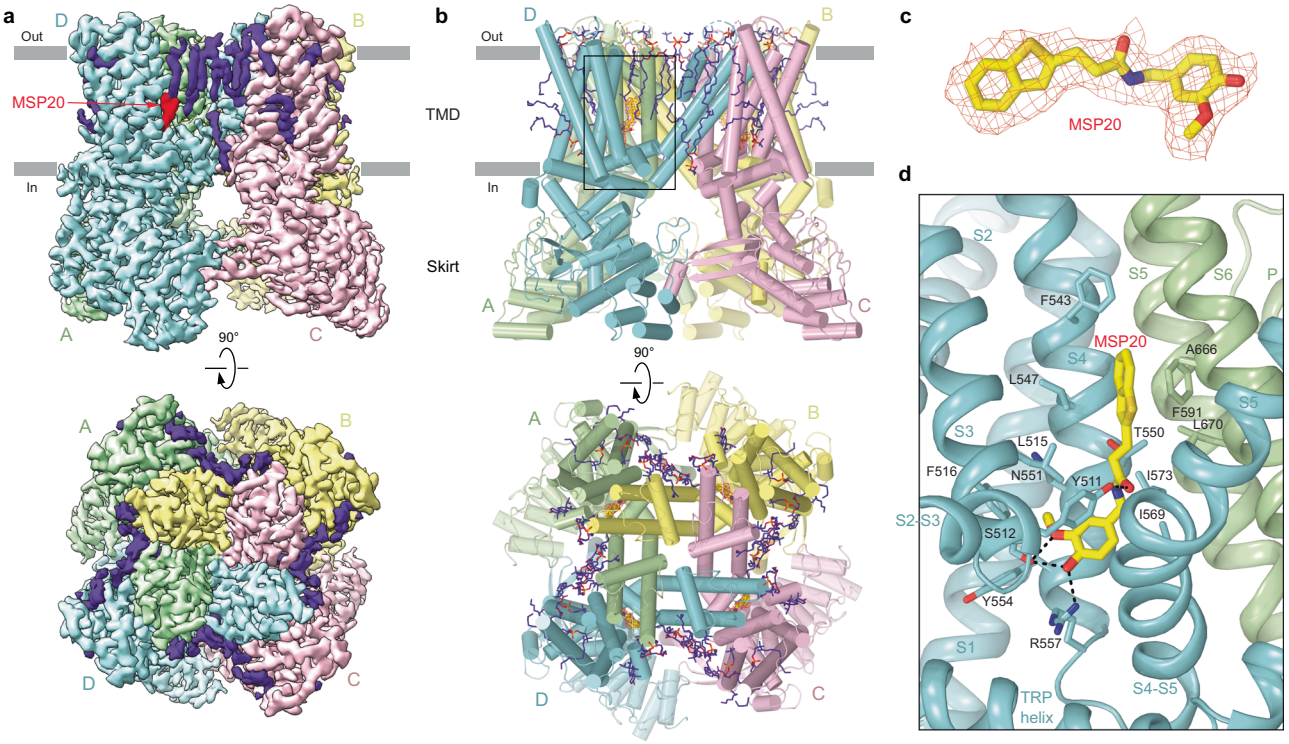

Fig. 6 | Structure of hTRPV1 in complex with MSP20. a 3D cryo-EM reconstruction of hTRPV1 in complex with MSP20 viewed parallel to the membrane (top) or extracellularly (bottom), with density for subunits coloured green, yellow, pink and blue, lipids in purple, and MSP20 in red. **b** $hTRPV1_{MSP20}$ structure coloured similarly to (**a**), with molecules of MSP20 and lipids shown as sticks. **c** Molecular model of MSP20, with the cryo-EM density shown as a red mesh. **d** Close-up view of the binding pocket, with MSP20 and residues that contribute to its binding shown as sticks. Hydrogen bonds are indicated by dashed lines.

stabilizing interactions with neighbouring residues (Fig. 9b, c). Hydrogen bonds (H-bonds) between N560 and Q561 in the last 100 ns of MD simulations (MDs) and a persistent H-bonds and salt bridges network between R579 and D576 contribute to this increased separation (Supplementary Fig. 10). Furthermore, the close spatial proximity of R557 to E570 facilitates the formation of H-bonds in both the open and MSP20-bound conformations (Fig. 9d–g).

Across the three simulated replicates, MSP20 shows a consistent pattern of interactions with key residues within the TRPV1 binding pocket. In one replicate, MSP20 interacts with R557 residue in 63% of the conformations analysed. Additionally, MSP20 forms stable hydrogen bonds with S512 and G590 for 90% and 68% of the simulation time, respectively. The benzothiophene ring also engages in a π–π interaction with F516 for 24% of the time. In the other two replicates, MSP20 displays further relevant contacts. It interacts with Y511, establishing an H-bond for approximately 86–87% and a π–π interaction for 40-48% of the MD simulations. Moreover, two water-mediated bridges are formed with T550 and N551, each present for more than 90% of the trajectory. Finally, the hydroxyl group of MSP20 interacts with R557 for 97–98% of the simulation time, reinforcing the interaction pattern observed experimentally (Fig. 9e). Analysis of the macroscopic conductance (Gmacro) along the pore over the entire simulation trajectory predicted by the HOLE program indicates that TRPV1 in its open conformation displays a higher conductance relative to $hTRPV1_{MSP20}$ (Fig. 9f, g). Specifically, the average Gmacro value is 630.14 pS for the open conformation, compared to 443.40 pS for $hTRPV1_{MSP20}$. This finding further supports the hypothesis that the latter adopts a more structurally constricted pore architecture.

Managing chronic pain effectively remains a significant challenge, with the current market largely reliant on medications that have existed for decades[54]. While opioids are powerful pain relievers, they disrupt normal brain function and carry a high risk of addiction[55]. An emerging alternative involves developing small molecules that target specific pain-related receptors, such as TRP channels[56]. Among these, thermo-TRPs like TRPV1, the first discovered member of the vanilloid subfamily, are especially promising due to their essential role in detecting temperature-related pain, a function vital for survival[56]. TRPV1 has been identified as a crucial sensor in neuropathic pain and brain inflammation, playing a key role in microglia-neuron signalling[57]. In addition to treating chronic and neuropathic pain and disorders related to body temperature regulation[58], there is an urgent need for selective, high-affinity TRPV1 modulators. This urgency stems from TRPV1's increasingly recognized involvement in various psychiatric conditions, including depression, anxiety, fear, emotional stress, and substance abuse[59–63]. The balance between library design, ADME profile optimization, and target selection is central to modern medicinal chemistry. Such approach enables more targeted synthesis, reduced time and costs and maximization of chances to identify molecules with desired properties.

Here we demonstrated the power of this approach by developing a set of benzothiophene-substituted vanilloid-site TRPV1 agonists, by applying computational methods and obtaining a class of benzothiophene-based TRPV1 agonists with strong binding and functional activity. Laboratory tests revealed that prolonged or repeated exposure to these compounds leads to calcium-dependent desensitization of TRPV1, rendering the receptor unresponsive to painful stimuli. Cryo-EM applied to hTRPV1 in the presence of the lead compound, MSP20, resolved the structure of a synthetic TRPV1 agonist in complex with the human receptor. The structure illustrates how MSP20 interacts with the vanilloid binding site and stabilizes a desensitized state of TRPV1, marked by the closed ion channel pore, α-helical C-terminal domain, and the distinct behaviour of surrounding lipid. Remarkably, MSP20 appeared to be selective for TRPV1 showing neither agonistic nor inhibitory activity

https://doi.org/10.1038/s41467-026-74972-3

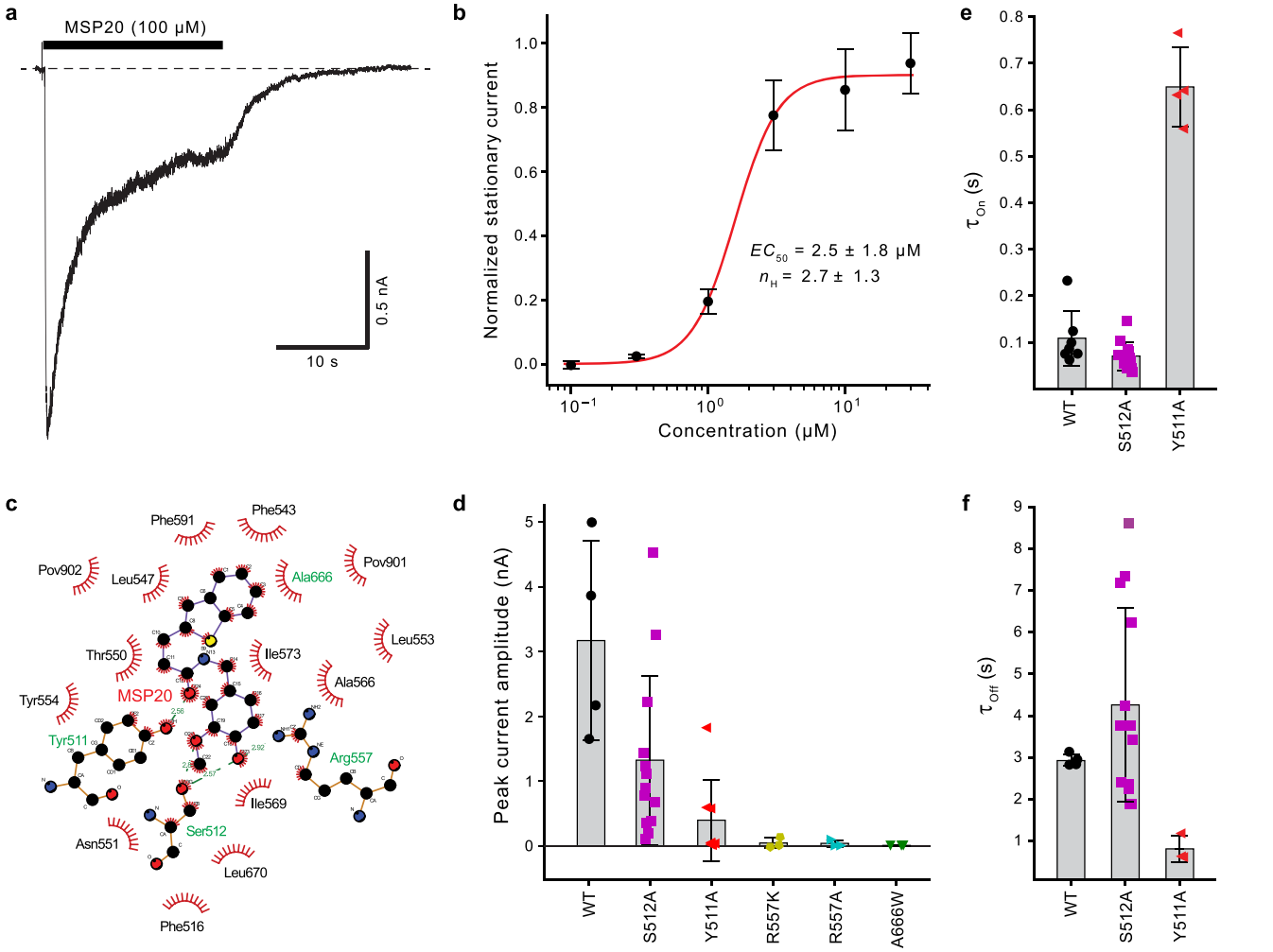

Fig. 7 | Electrophysiological characterization of human TRPV1 and MSP20 binding-pocket mutants. a Representative current trace illustrating pronounced desensitization of human TRPV1 in response to a 20-s application of MSP20 (100 μM). **b** Concentration dependence of steady-state currents elicited by MSP20. Currents were normalized to the maximal response obtained for each cell from fits to a Hill equation ($n = 5$ cells). Data points represent mean ± s.e.m. for each concentration. The legend reports the mean ± s.d. of fit parameters obtained from individual cells. **c** LigPlot representation of the MSP20 binding pocket. Residues selected for mutagenesis are highlighted in green. **d** Peak current amplitudes recorded from WT TRPV1 and MSP20 binding-pocket mutants using a 5-s agonist application protocol ($n_{WT} = 4$, $n_{S512A} = 13$, $n_{Y511A} = 8$, $n_{R557K} = 3$, $n_{R557A} = 3$, $n_{A666W} = 3$). *P* values were obtained using two-sided Student's *t* test comparing WT with each mutant: S512A, $P = 0.031$; Y511A, $P = 0.001$; R557K, $P = 0.019$; R557A, $P = 0.019$; A666W, $P = 0.018$. **e** Activation (on) kinetics of WT TRPV1 and mutants exhibiting measurable MSP20-evoked currents ($n_{WT} = 7$, $n_{S512A} = 13$, $n_{Y511A} = 4$). *P* values from two-sided Student's *t* test comparing WT with mutants: S512A, $P = 0.064$; Y511A, $P = 5.1 \times 10^{-7}$. **f** Deactivation (off) kinetics of WT TRPV1 and mutants exhibiting measurable MSP20-evoked currents ($n_{WT} = 4$, $n_{S512A} = 13$, $n_{Y511A} = 3$). *P* values from two-sided Student's *t* test comparing WT with mutants: S512A, $P = 0.283$; Y511A, $P = 7.1 \times 10^{-5}$. Bars and whiskers in **d**–**f** indicate mean and s.d., respectively.

on other TRP channels, namely TRPA1, TRPM8, TRPV3 and TRPV4. In vitro results indicate that MSP20 is a non-cytotoxic compound that effectively reduces GO-induced ROS production in HaCaT- and HUVEC-cells, suggesting its potential therapeutic application in oxidative stress-related conditions. In vivo and ex vivo studies showed that MSP20 provides strong pain relief and neuroprotection, respectively, highlighting the potential of this class of benzothiophene-derived compounds as effective analgesics with long-lasting and protective benefits. Intriguingly, the availability of a less potent agonist (MSP20 *vs* capsaicin) that also lacks effects on body temperature could offer an advantage for chronic treatment, as well demonstrated by the long-term use of other analgesics in first-line therapy for pain management[64]. Overall, the data presented here underline the validity of the benzothiophene-substituted scaffold as a template for the rational design and synthesis of potent TRPV1 modulators to develop the next generation of urgently needed analgesics. Moreover, these findings encourage a deeper investigation into the biological properties of our lead compound, MSP20, as well as the additional pathways potentially involved.

Methods

Ethical statement

The authors confirm that this research complies with all relevant ethical regulations. The board/committee and institution that approved the study protocols are reported in the appropriate paragraphs of this section.

In silico lead optimization

For the molecular modelling studies, we employed the cryo-EM structure of hTRPV1 in complex with (2*E*)-3-(4-chlorophenyl)-*N*-(3-methoxyphenyl)prop-2-enamide (SB-366791), a TRPV1-specific nanomolar-affinity analgesic antagonist, available in the Protein Data Bank (PDB) under the code 8GFA[16]. The receptor structure was processed using the Protein Preparation Wizard tool in Maestro,

https://doi.org/10.1038/s41467-026-74972-3

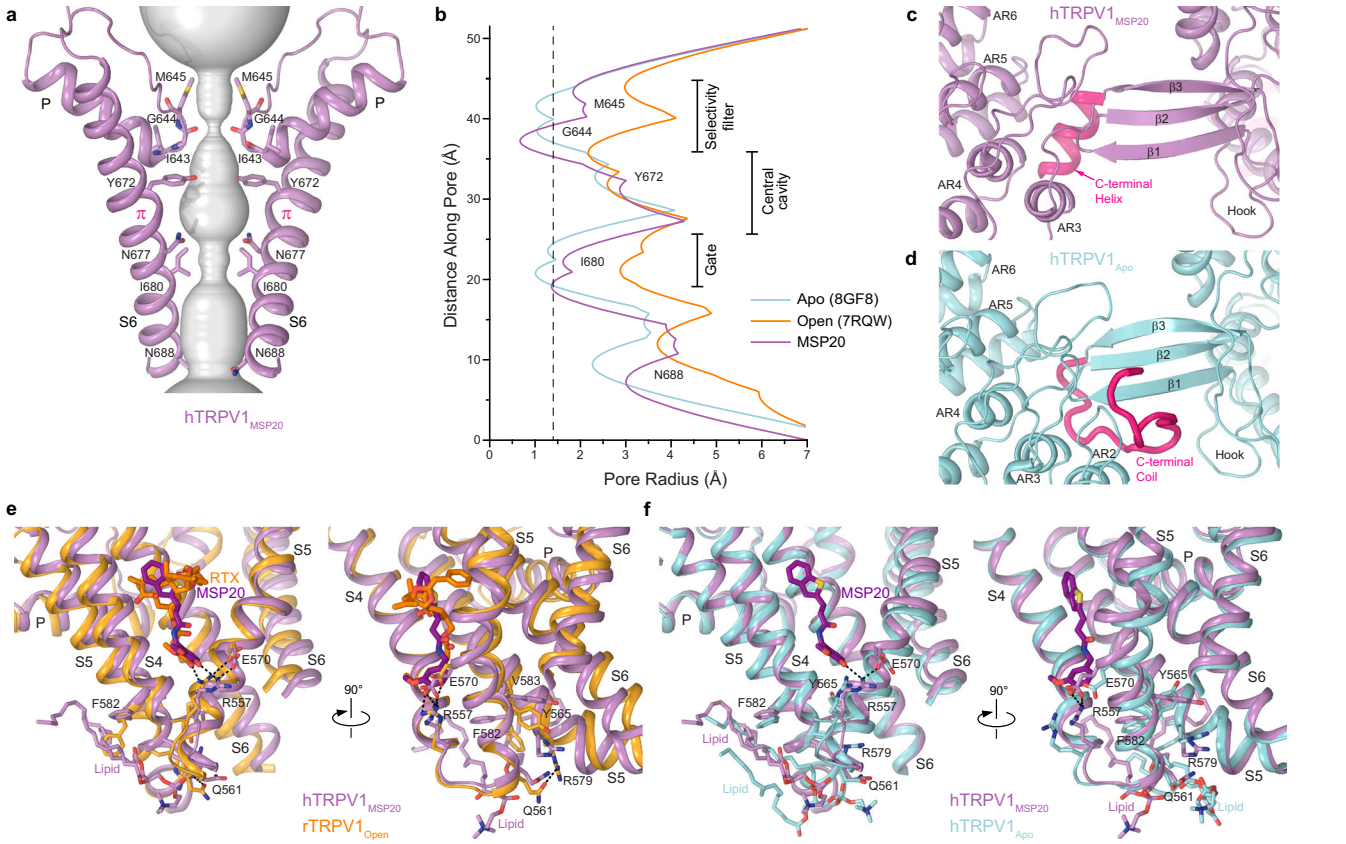

Fig. 8 | Comparison of the MSP20-bound, closed apo and open state TRPV1 structures. a Pore-forming domain in $hTRPV1_{MSP20}$ with the residues contributing to pore lining shown as sticks. Only two of four subunits are shown, with the front and back subunits omitted for clarity. The pore profile is shown as a space-filling model (grey). The region that undergoes α-to-π transition in S6 is labelled (*π*). **b** Pore radius for $hTRPV1_{Apo}$ (cyan; PDB ID: 8GF8), $rTRPV1_{Open}$ (orange; PDB ID: 7RQW), and $hTRPV1_{MSP20}$ (violet) calculated using HOLE. The vertical dashed line denotes the radius of a water molecule, 1.4 Å. **c**, **d** Interface between the neighbouring subunits in $hTRPV1_{MSP20}$ (**c**) and $hTRPV1_{Apo}$ (**d**), with the C-terminus (pink) adapting helical (**c**) and coiled (**d**) conformations. **e**, **f** Closeup view of the vanilloid site in superposed $hTRPV1_{MSP20}$ and $rTRPV1_{Open}$ (**e**) or $hTRPV1_{MSP20}$ and $hTRPV1_{Apo}$ (**f**), with strong electrostatic interactions indicated by dashed lines.

adopting the OPLS_2005 force field (Protein Preparation Wizard; Schrödinger, LLC: New York, NY, USA, 2018)[65]. Crystallographic buffer components, water molecules, and phosphate ions were removed; hydrogen atoms were added, side-chain protonation states adjusted to pH 7.4, and energy minimization conducted. The library of heterocyclic compounds was generated by means of Ligand Designer, and their pharmacokinetic properties were assessed using QikProp (Schrödinger Release 2020-4: QikProp, Schrödinger, LLC, New York, NY). Refinement was performed by eliminating chiral centres, discarding molecules that violated Lipinski's Rule of Five or Rule of Three, and excluding those containing reactive groups. Only compounds predicted to cross BBB were retained, selecting candidates with a CNS parameter greater than −1. For docking studies, Glide software (version 8.9; Schrödinger Release 2020-4: Glide, Schrödinger, LLC, New York, NY) was employed[66]. The receptor grid was built through Receptor Grid Generation with the OPLS_2005 force field, centred on the co-crystallized ligand, and configured with a grid box size of 10 × 10 × 10 Å. Docking simulations were carried out using the standard precision (SP) algorithm, yielding 10 poses per ligand. To validate the reliability of the docking protocol, re-docking of the co-crystallized ligand was performed. The root mean square deviation (RMSD) values between the experimental ligand pose and the predicted docking conformations were analysed to assess the protocol's capability to replicate the experimentally determined binding mode. Compounds with better scores with respect to the docking threshold were subsequently subjected to MM/GBSA analysis to identify benzo-fused heterocyclic based compounds that optimize binding pocket entry and enhance molecular interactions.

Synthesis of amides 2-9

Method A (compounds 6 and 8)

To a stirred mixture of the appropriate amine hydrochloride (0.728 mmol, 1.5 eq., 4-hydroxy-3-methoxybenzylamine hydrochloride for **6** and 2-(3,4-dihydroxyphenyl)ethylamine hydrochloride for **8**) and triethylamine (0.970 mmol, 2.0 eq.) in anhydrous ACN (20 mL), a solution of the 3-(benzo[*b*]thiophen-2-yl)propanoic acid (0.485 mmol, 1.0 eq.) in the same solvent (5 mL), HOBt (0.582 mmol, 1.2 eq.), and EDC (0.728 mmol, 1.5 eq.) were added in this order, maintaining the reaction at room temperature (RT) and under nitrogen atmosphere for 16 h. After this time, the solvent was removed under reduced pressure and the residue taken up with EtOAc. The organic layer was washed with a saturated NH_4Cl solution (2 × 10 mL), then with brine (2 × 10 mL), and finally dried over Na_2SO_4. Filtration and evaporation of the solvent afforded a crude residue which was purified by flash chromatography on silica gel with the appropriate eluent.

Method B (compounds 2-5, 7 and 9)

To a solution of the appropriate amine (0.728 mmol, 1.5 eq., 4-aminophenol for **2**, benzylamine for **3**, 4-methoxybenzylamine for **4**, 4-hydroxybenzylamine for **5**, 3,4-dichlorobenzylamine for **7**, 3-chloro-4-methoxyphenetylamine for **9**) in anhydrous DCM (25 mL, **3**, **4**, **7** and **9**) or anhydrous ACN (HPLC grade, 30 mL, **2** and **5**) a solution of the 3-(benzo[*b*]thiophen-2-yl)propanoic acid (0.485 mmol, 1.0 eq.) in the

https://doi.org/10.1038/s41467-026-74972-3

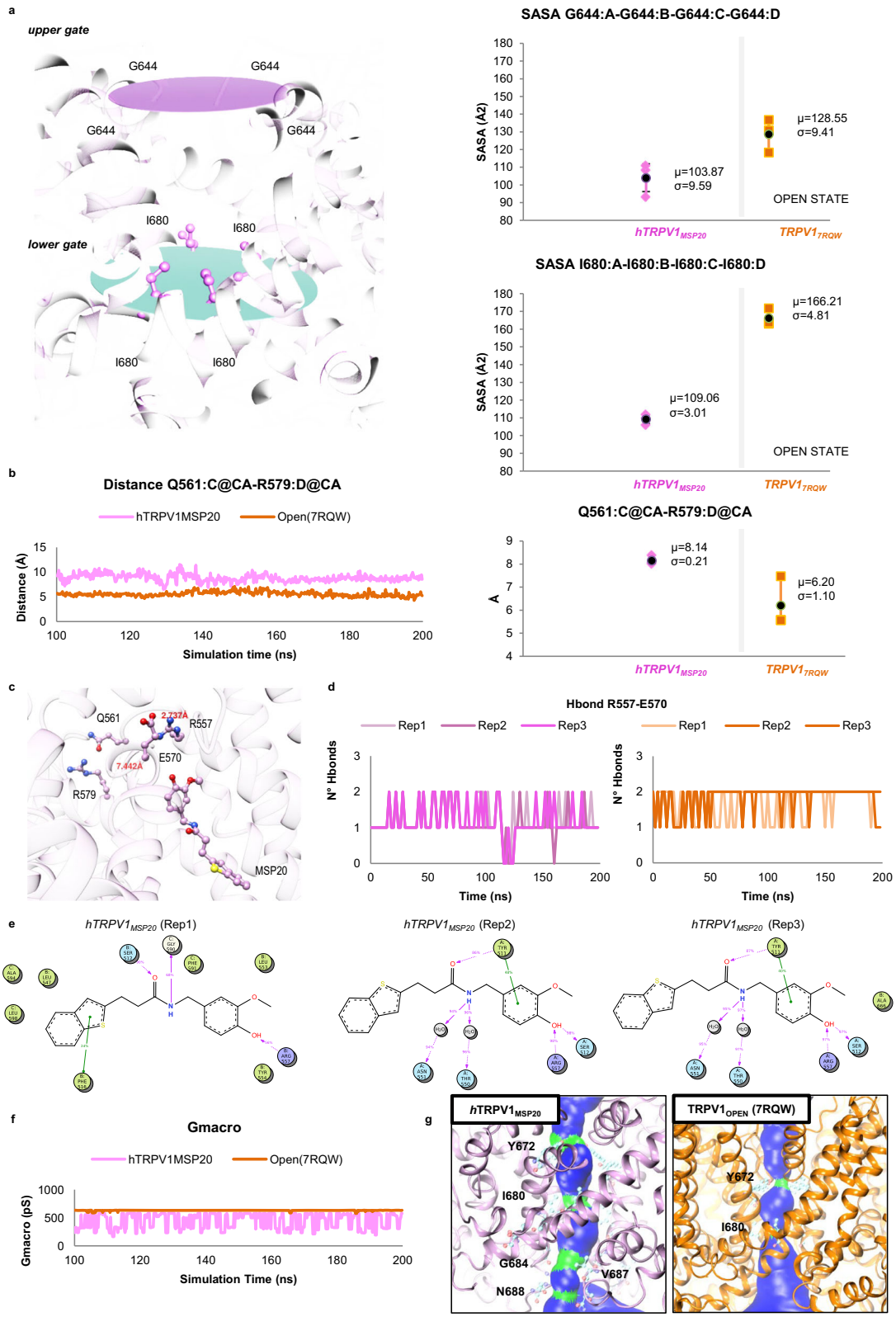

same solvent (5 mL), HOBt (0.582 mmol, 1.2 eq.) and EDC (0.728 mmol, 1.5 eq.) were added in this order, maintaining the reaction at RT and under nitrogen atmosphere overnight. After this time, reaction mixture in ACN was concentrated under reduced pressure and the residue taken up with EtOAc, while reaction mixture in DCM was used as such. The organic layer was washed with a saturated NH_4Cl solution (2 × 10 mL), then with brine (2 × 10 mL), and finally dried over Na_2SO_4. Filtration and evaporation of the solvent afforded a crude residue which was purified by flash chromatography on silica gel with the appropriate eluent.

3-(Benzo[*b*]thiophen-2-yl)-*N*-(4-hydroxybenzyl)propanamide (5) Amide **5** can also be obtained from compound **4** (0.154 mmol, 1.0 eq.) dissolved in dry toluene (1 mL) and treated with BBr_3 (0.616 mmol,

Fig. 9 | Molecular dynamic simulations of the hTRPV1$_{MSP20}$ and rTRPV1$_{Open}$ complexes. a 3D representation of the TRPV1 pore with G644 (upper gate) and I680 (lower gate) residues (shown as CPK) marked as violet and turquoise area, respectively. Solvent accessible surface area (SASA), expressed in Å^2, of G644 and I680 interfacial residues participating in the pore-forming domain, along the last 100 ns of MDs. Boxplots display the average (μ), standard deviation (σ) of three independent 200 ns of MDs for each system. **b** Plot of the distance between Cα of Q561 and R579 along the last 100 ns of MDs in the presence of MSP20 and in the TRPV1 open-state conformation. Boxplots display the average (μ), standard deviation (σ) of three independent 200 ns of MDs for each system. **c** Closeup view of the vanilloid site in hTRPV1$_{MSP20,}$ with the key residues and the ligand depicted in CPK. **d** H-bonds monitoring between R557 and E570 along the three independent 200 ns of MDs for each system. **e** 2D interaction diagrams of MSP20 in complex with TRPV1 for each simulated replicate. The charged positive, the hydrophobic, the polar and neutral residues are shown as blue, green, cyan, and white spheres. The pink and the green lines depict hydrogen bonds and π−π interactions, respectively, followed by the related percentage of occurrence during the last 100 ns of three independent MDs. **f** Conductance (Gmacro), expressed in pS, along the last 100 ns of MDs. **g** Pore-forming domain of the last snapshot of hTRPV1$_{MSP20}$ and open (7RQW) MDs with the residues contributing to pore lining shown as CPK. The green surface is where the pore radius is proper for a single water, while the blue surface is where the radius is double the minimum for a single.

60.0 μL, 4.0 eq.). The mixture was heated at 50 °C for 15 minutes then stirred at 100 °C for 1 h. After cooling to RT, the reaction mixture was first washed with brine (2 × 10 mL) and then treated with 2 N NaOH aqueous solution. The basic phase was acidified with 12 N HCl until pH = 2 and then extracted with Et_2O (3 × 15 mL). The collected organic layers, dried over anhydrous Na_2SO_4, were concentrated and pure compound was isolated as white solid, yield 20.0%.

Materials, characterization data, ^{1}H and ^{13}C NMR traces, LC-MS chromatograms and HRMS analysis of compounds **2-9** are available in the Supplementary Information.

Fluorescent measurements of intracellular calcium concentration

HEK 293 cells (CRL-1573, ATCC, Manassas, VA, USA) stably overexpressing recombinant hTRPV1, rTRPA1, rTRPM8, rTRPV3 and rTRPV4 were loaded with the methyl ester of Fluo-4-AM (4 μM, Invitrogen), as described[67], and the effect of test compounds was determined by evaluating the intracellular calcium ion concentration ($[Ca^{2+}]_i$). Indeed, by measuring cell fluorescence at RT (λ_{EX} = 488 nm, λ_{EM} = 516 nm), $[Ca^{2+}]_i$ was evaluated before and after the addition of various concentrations of the test compounds, taking the values of the effect on $[Ca^{2+}]_i$ in wild-type HEK 293 cells as baseline and subtracted from the values obtained from transfected cells. The efficacy of the compounds was determined by normalizing their effect to the maximum Ca^{2+} influx effect on $[Ca^{2+}]_i$ observed with application of 4 μM ionomycin. The effects of TRPA1 agonists are expressed as a percentage of the effect obtained with 100 μM allyl isothiocyanate (AITC). In the TRPV3 assay, the cells were first sensitized with the structurally unrelated agonist 2-aminoethoxydiphenyl borate (100 μM). For the TRPM8, the experiments were carried out at 22 °C. Potency (EC_{50}) was expressed as the concentration of test compound exerting a half-maximal agonist effect (*i.e.*, half-maximal increases $[Ca^{2+}]_i$) while antagonist/desensitizing behaviour was evaluated against capsaicin (0.1 μM) for TRPV1, AITC (100 μM) for TRPA1, icilin (0.25 μM) for TRPM8, thymol (100 μM) for TRPV3 and GSK1016790A (10 nM) for TRPV4 by adding each test compound in the quartz cuvette 5 min before stimulation of cells with agonists. The effect on $[Ca^{2+}]_i$ exerted by the agonist alone was taken as 100% and data are expressed as the concentration exerting a half-maximal inhibition of agonist-induced $[Ca^{2+}]_i$ elevation (IC_{50}). Curve fitting (sigmoidal dose-response variable slope) and parameter estimation were performed with GraphPad Prism (version 9.2.0, GraphPad Software Inc., San Diego, CA) and all determinations were performed at least in triplicate.

Keratinocyte and endothelial cell culture, treatment, ROS- and viability-assay

HaCaT (spontaneously immortalized, human keratinocyte) cells purchased from ThermoFisher Scientific (Addexbio Technologies, T0020001, Waltham, MA, USA) were cultured in Dulbecco's Modified Eagle's Medium (DMEM) High Glucose (Lonza, Milan, Italy), supplemented with 10% foetal bovine serum (FBS), 100 U/mL penicillin, 100 μg/mL streptomycin, and 2 mM L-glutamine (Hyclone, Euroclone, Milan, Italy), as previously described[68]. Human umbilical vein endothelial cells (HUVEC) were purchased from ThermoFisher Scientific (Gibco Cat#C0035C, Waltham, MA, USA). They were grown in endothelial growth medium (EGM-2), containing VEGF, R3-IGF-1, hEGF, hydrocortisone, ascorbic acid, heparin and GA-1000 (Lonza, Milan, Italy) and supplemented with 10% foetal bovine serum (FBS) (Hyclone, Euroclone, Milan, Italy). Cells were split 1:3 twice a week and used until passage 8. Cells were maintained at 37 °C in a humidified atmosphere of 95% air/5% CO_2 and allowed to reach 80% confluence before treatment. MSP20 was dissolved in ethanol (EtOH) to prepare a 10 μM stock solution, which was subsequently diluted in culture medium to the required concentrations. The final concentration of EtOH in the culture medium did not exceed 0.1% (v/v). For compounds treatment, either HaCaT and HUVEC cells were incubated with MSP20 at various concentrations for 24 or 48 hours. Cell viability was assessed using the Alamar Blue (resazurin sodium salt) and lactate dehydrogenase (LDH) release (EuroClone, Milan, Italy) assays at 24- and 48-hours post-treatment. LDH release was enzymatically measured as previously described[12]. As a positive control for 100% toxicity, cells were lysed with 0.1% (v/v) Triton X-100 in culture medium for 30 minutes at 37 °C. For Alamar Blue staining, a stock solution of resazurin (1 mg/mL) in phosphate-buffered saline (PBS, pH 7.4) was diluted to a final working concentration of 0.1 mg/mL in culture medium. The redox indicator was measured at 544 nm excitation and 590 nm emission to evaluate its oxidized versus reduced forms (TECAN Infinite M200 plate reader). For the assessment of reactive oxygen species (ROS) production, cells were exposed to glucose oxidase (GO, 1 U/mL, 1 h) following MSP20 treatment. Intracellular ROS levels were measured using the dichlorofluorescein diacetate (DCFH-DA) assay. Both HaCaT and HUVEC cells (5 × 10^4 cells/mL) were pretreated with MSP20 at different concentrations (0.1-100 μM) for 24 hours, followed by incubation with 20 μM DCFH-DA in loading medium at 37 °C for 30 minutes in a 95% air/5% CO_2 environment. After this, cells were exposed to GO for 30 minutes, and fluorescence intensity was recorded at 485 nm excitation and 530 nm emission (TECAN Infinite M200 plate reader). Data were expressed as percent value of GO fluorescence. Untreated-(control) and solvent (EtOH)-treated cells percent fluorescence values were: HaCaT, 4.62 ± 0.87 % (control), 2.01± 0.05 % (EtOH). HUVEC, 6.26 ± 1.21% (control), 5.24 ± 0.15% (EtOH) vs GO.

Absorption, distribution, metabolism, and excretion (ADME) studies

Reagents and solvents were purchased from Sigma-Aldrich Srl (Milan. Italy) and Carlo Erba Reagents Srl (Milan, Italy). Milli-Q quality water (Direct-Q®, Merck, Darmstadt, Germania).

The chromatographic studies were carried out using an Agilent 1260 LC/MSD VL system (G1946C) (Agilent Technologies, Palo Alto, CA), which included a vacuum solvent degassing unit, a binary high-pressure gradient pump, and a 1260 series UV detector. The Agilent 6130 series mass spectra detection (MSD) single-quadrupole instrument was outfitted with the orthogonal spray API-ES (Agilent Technologies, Palo Alto, California). Nitrogen was utilized as a nebulizing

and drying gas. The MS conditions used for signal acquisition were as follows: drying gas flow rate and temperature of 5 L/min and 300 °C, nebulizer pressure of 60 psi, and vaporizer temperature set to 150 °C. Phenomenex Kinetex C18 column (150 mm × 4.6 mm, 5 μm particle size) was used for chromatographic separation at RT, followed by gradient elution with a binary solution (Supplementary Table 5), using a flow rate of 0.6 mL/min and a reference wavelength of 254 nm and a MS range of acquisition between 100 and 1000 m/z both in positive and negative mode using a collision energy of 70 eV.

Thermodynamic aqueous solubility

A suitable volume of water Milli-Q was added to the solid compound to reach a final concentration of 1.0 mg/mL. The solution was mixed and stirred overnight at RT with a microplate shaker. After incubation, the suspension was filtered using a 0.45 μm PTFE filter (VWR). The filtered solution was analysed to quantify the solubilized component using the UV/LC-MS method described above and compared to the appropriate calibration curve.

Parallel artificial membrane permeability assay (PAMPA)

The PAMPA assay across the GI and BBB was carried out preparing "donor" and "acceptor" solutions. First, each compound's DMSO stock solution was diluted $1{:}1_{v/v}$ with phosphate buffer (PBS 10 mM, pH 7.4), while the "acceptor" solution was a $1{:}1_{v/v}$ DMSO/PBS solution. To replicate the gastrointestinal and BBB phospholipidic bilayers, each well of the filter plate was coated with a $1\%_{w/v}$ L-α-phosphatidylcholine solution (PC) in dodecane or a $10\%_{w/v}$ $CHCl_3$/dodecane brain polar lipid solution. The donor solution was then applied. The DMSO/PBS $1{:}1_{v/v}$ solution was placed into the acceptor plate, and the sandwich was incubated for 5 hours at RT with gentle shaking. After the incubation time, the samples were collected and analysed using the HPLC-UV/MS method reported before and the apparent permeability ($P_{app} \times 10^{-6}$ cm/s) was calculated as reported by us[69].

Metabolic stability in human liver microsomes (HLMs)

A DMSO solution of each compound tested was incubated at 37 °C for 1 hour in phosphate buffer (10 mM, pH 7.4), human liver microsomes (0.20 mg/mL), and a NADPH regenerating system (NADPH 0.2 mM, $NADPH^+$ 1 mM, D-glucose-6-phosphate 4 mM, 4 unit/mL glucose-6-phosphate dehydrogenase) in $MgCl_2$ 48 mM at a final volume of 0.5 mL. After incubation, the reaction was stopped using 1.0 mL of acetonitrile. The mixture was then centrifuged at 3510 × *g* for 10 minutes, and the supernatant was collected and analysed using the appropriate LC-UV/MS technique. The percentages of the metabolized and unmetabolized compounds were calculated as previously described[70]. The metabolic stability of each compound was determined in triplicate and through three independent tests.

Plasma stability studies

The plasma stability studies were carried out by incubating the tested compound (2.0 mM) with pooled human plasma (1.0 mL, 55.7 mg protein/mL) and HEPES buffer (25 mM, 140 mM NaCl pH 7.4). At selected time points (0, 0.083, 0.25, 0.5, 1, 2, 6, 24 h), samples were collected and treated with cold acetonitrile to stop the action of esterases. The reaction mixture was then centrifugated (3510 × *g* for 10 min) and the supernatant was collected and analysed using the LC-UV/MS previously reported and it was quantified as the unmodified compound. The half-life was calculated with the following formula:

$$t_{1/2} = 0.693/b \quad (1)$$

Where b is the slope found in the linear fit of the natural logarithm of the fraction remaining of the parent compound *vs.* incubation time. The plasma stability determination was performed for each compound in three independent experiments.

DPPH and ABTS antioxidant assay

The antioxidant activity of MSP20 was investigated using two well-known methods: DPPH (2,2-diphenyl-1-picrylhydrazyl) radical scavenging assay, and ABTS (2,2'-azino-bis(3-ethylbenzothiazoline-6-sulphonic acid) radical cation (ABTS+) decolorization assay. Both assays were performed as reported elsewere[71]. Briefly, for the DPPH assay, 100 μL of the MSP20 and the reference compound (capsaicin) at scalar concentrations (50–2000 μM) were added to 1.0 mL of 0.2 mM DPPH methanolic solution, followed by 1.9 mL of MeOH. The mixtures were incubated for 30 minutes in the dark at RT and then the absorbance was measured at 517 nm (UV/visible Lambda 2 spectrophotometer, Perkin Elmer, Norwalk, CT, USA). For the ABTS assay, 100 μL of the tested compound and capsaicin, at the same concentrations reported above, were added to 1.5 mL of ABTS solution followed by 1.4 mL of EtOH. The mixtures were left to react for 10 min in the dark at RT. The absorbance was measured at 751 nm (UV/visible Lambda 2 spectrophotometer, Perkin Elmer, Norwalk, CT, USA). For both assays, we used Trolox as standard compound and a mixture of MeOH or EtOH with compounds as blank. All the experiments were repeated six times ($n = 6$) and the results are expressed as EC_{50} defined as the concentration of the compound which achieved the effect of scavenging 50% of free radicals initially formed following ABTS and DPPH assay.

Evaluation of neuroprotection in rat brain slices

All animal care and experimental protocol conformed to the European Union Guidelines for the Care and the Use of Laboratory Animals (European Union Directive 2010/63/EU) and was approved by the University of Siena Animal Welfare Body and the Italian Ministry of Health (7DF19.N.TBT). Details were previously reported in references[12,21,72]. In brief, experiments were performed by using male Wistar rats (Charles River, Calco, Italy) housed in cages of 3–4 animals at constant temperature (22 ± 2 °C) and humidity (55 ± 10%) with a 12 h reverse light/dark cycle and free access to food and water. Cortical slices (400 μm) from male Wistar rats were initially placed in artificial cerebrospinal fluid (ACSF, composition in mM: 120 NaCl, 2 KCl, 1 $CaCl_2$, 1 $MgSO_4$, 25 HEPES, 1 KH_2PO_4, and 10 glucose, final pH 7.4, continuously bubbled with a gas mixture of 95% O_2 and 5% CO_2) and left at room temperature in ACSF for 30 minutes to recover from mechanical stress (equilibration phase 1). Subsequently, they were transferred to 24-well culture plates (2–3 slices/well, mean weight ~30–40 mg) containing 0.5 mL ACSF at 37 °C and maintained for an additional 60 minutes (equilibration phase 2), with the medium being replaced every 15 minutes with fresh, oxygenated ACSF. Following equilibration phase 2, slices were subjected to the pre- and co-treatment protocol (see Supplementary Fig. 11 for details), i.e., they were treated with ACSF (controls) or compounds for 60 minutes before being exposed to glutamate (60 mM for another 120 minutes, a procedure known to induce approximately 50% tissue death[21]) or glutamate plus compounds. Fresh glutamate solutions were prepared as 500 mM stock solution in 1 M HCl, which was re-equilibrated at pH 7.5 before dilution to 50 mM working concentrations with ACSF immediately before use. Upon completion of the treatments, tissue viability was evaluated using the colorimetric MTT (3-(4,5-dimethylthiazol-2-yl)-2,5-diphenyltetrazolium bromide) method, taking viability of control slices as 100%[73].

Evaluation of antinociceptive activity in mice by the formalin test

All experiments were conducted in accordance with the National Institutes of Health Guidelines for the Care and Use of Laboratory Animals, with efforts made to reduce both the number of animals used and their discomfort. The study protocol was reviewed and approved by the Ethics Committee of the University of Campania 'Luigi Vanvitelli' (Naples, Italy) and authorized by the Italian Ministry of Health (Protocol No. 806/2023). Male C57BL/6J mice (8 weeks old at arrival) were obtained from Inotiv Inc. and were group-housed and maintained

under controlled illumination (12 h light/dark cycle) and standard environmental conditions (ambient temperature 20–22 °C, humidity 55–60 %). Food and water were available ad libitum. Each mouse was randomly assigned to one of the experimental groups, placed in a plastic cage, and allowed to move freely for 30 min. A mirror was placed at a 45° angle under the cage to allow a full view of the hind paws. Vehicle (5% DMSO and 0.9% saline) or different doses of MSP20 (0.0075 μg/paw, 0.015 μg/paw, 0.15 μg/paw, 30 μL) were subcutaneously administered 10 min before injecting formalin (1.25%, 30 μL) into the dorsal surface of the hind-paw. Lifting, licking, shaking, and flinching of the injected paw were recorded as nocifensive responses. Recording of nocifensive behaviour, scored in 5-min blocks, commenced immediately after the injection of formalin and was continued for 60 min. Groups of 10 mice per treatment were used, with each animal used for one treatment only. The behavioural experiments were conducted blindly, and thresholding and data analysis were unaware of treatment allocation. Results have been expressed as mean ± S.E.M. of the total time spent in nocifensive response in sec. Behavioural data were analysed by two-way ANOVA followed by Dunnet's post-hoc test. Statistical analysis was carried out using Prism/Graphpad (GraphPad Software, Inc.) software.

Assessment of body temperature in mice

Body temperature was measured using a rectal thermocouple probe connected to a digital thermometer[40,74]. Male C57BL/6J mice (8 weeks old at arrival) were obtained from Inotiv Inc. and were group-housed and maintained under controlled illumination (12 h light/dark cycle) and standard environmental conditions (ambient temperature 20–22 °C, humidity 55–60 %). Food and water were available ad libitum. Mice ($n = 8$ per group) were randomly assigned to one of the experimental groups and briefly restrained using a handling tunnel to minimize stress-induced hyperthermia. The probe was inserted 2 cm into the rectum and held in place until a stable temperature reading was obtained. Measurements were taken at baseline (pre-treatment) and 30, 60, 90, 120 and 150 minutes following subcutaneous injection of MSP20 (7 mg/kg, dissolved in 5% DMSO and 0.9% saline) administered in the dorsal neck region. For chronic measurement, mice ($n = 5$ per group) were randomly assigned to one of the experimental groups and body temperature was taken at baseline, 1, 3 and 7 days with daily treatment. Between measurements, mice were returned to their home cages. The probe was thoroughly cleaned with 70% ethanol after each measurement to prevent cross-contamination. Behavioural experiments were conducted blindly, and thresholding and data analysis were unaware of treatment allocation.

Spared nerve injury (SNI) induction and mechanical allodynia measurement

The Spared Nerve Injury (SNI) pain model was induced in C57 mice according to established protocols[41]. All experiments were conducted in accordance with the National Institutes of Health Guidelines for the Care and Use of Laboratory Animals, with efforts made to reduce both the number of animals used and their discomfort. The study protocol was reviewed and approved by the Ethics Committee of the University of Campania 'Luigi Vanvitelli' (Naples, Italy) and authorized by the Italian Ministry of Health (Protocol No. 806/2023). Male C57BL/6J mice (8 weeks old at arrival) were obtained from Inotiv Inc. and were group-housed and maintained under controlled illumination (12 h light/dark cycle) and standard environmental conditions (ambient temperature 20–22 °C, humidity 55–60 %). Food and water were available ad libitum. Briefly, each mouse was randomly assigned to one of the experimental groups and surgical anaesthesia was achieved and maintained using isoflurane (3% for induction, 1.5% for maintenance in oxygen). Following a skin incision, the sciatic nerve and its three terminal branches, the sural, tibial, and common peroneal nerves, were carefully isolated. The tibial and common peroneal nerves were then ligated using 5-0 silk suture and sectioned. The Von Frey behavioural test has been performed to evaluate the development of mechanical allodynia following the injury induction and behavioural experiments were conducted blindly and thresholding and data analysis were unaware of treatment allocation. The treatment was initiated after SNI surgery, following the recovery period, via subcutaneous injection of MSP20 (7 mg/kg) into the dorsal neck region, or vehicle (5% DMSO in 0.9% saline), for up to 7 days. The dose of MSP20 was selected based on the literature[74]. Mice were placed in individual enclosures on an elevated wire mesh floor and allowed to habituate for 60 minutes. Mechanical sensitivity was assessed using a series of Von Frey filaments (Ugo Basile, Varese, Italy) with logarithmically increasing stiffness (ranging from 0.008 to 2.0 g). Filaments were applied perpendicularly to the plantar surface of the hind paw with sufficient force to cause a slight bend, following an up-down paradigm. Each filament was tested three times in succession. A positive withdrawal response was defined as a sharp lifting, licking, or shaking of the paw immediately upon filament application[75].

Protein expression and purification for cryo-EM

Human TRPV1 was expressed and purified as previously described in detail for TRPV3[76–78] with slight modifications. In short, bacmids and baculoviruses were produced using a standard method[79]. Baculovirus was made in Sf9 cells (Thermo Fisher Scientific, mycoplasma test negative, GIBCO #12659017) for ~72 hours and was added to suspension-adapted HEK 293S cells lacking N-acetylglucosaminyltransferase I (GnTI$^-$, mycoplasma test negative, ATCC #CRL-3022) that were maintained at 37 °C and 5% CO_2 in Freestyle 293 media (Gibco-Life Technologies #12338-018) supplemented with 2% FBS. To enhance protein expression, sodium butyrate (10 mM) was added 24 hours after transduction and the temperature was reduced to 30 °C. At 48–72 hours post-transduction, the cells were harvested by centrifugation at 5471 × *g* for 15 min using a Sorvall Evolution RC centrifuge (Thermo Fisher Scientific), washed in phosphate buffer saline (PBS) pH 8.0, and pelleted by centrifugation at 3202 × *g* for 10 min using an Eppendorf 5810 centrifuge. The cell pellet was resuspended in the ice-cold buffer containing 20 mM Tris pH 8.0, 150 mM NaCl, 0.8 μM aprotinin, 4.3 μM leupeptin, 2 μM pepstatin A, 1 μM phenylmethylsulfonyl fluoride (PMSF), and 1 mM β-mercaptoethanol (βME). The suspension was then supplemented with 1% (w/v) n-dodecyl-β-D-maltoside (DDM), and cells were lysed at constant stirring for 2 hours at 4 °C. Unbroken cells and cell debris were pelleted in an Eppendorf 5810 centrifuge at 3202 × *g* and 4 °C for 10 min. Insoluble material was removed by ultracentrifugation for 1 hour at 186,000 × *g* in a Beckman Coulter centrifuge using a Type 45 Ti rotor. The supernatant was added to the strep resin, which was then rotated for 1 hour at 4 °C. The resin was washed with 10 column volumes of wash buffer containing 20 mM Tris pH 8.0, 150 mM NaCl, 1 mM βME, and 0.01% (w/v) glyco-diosgenin, and the protein was eluted with the same buffer supplemented with 2.5 mM D-desthiobiotin. The eluted protein was concentrated to 0.5 mL using a 100-kDa NMWL centrifugal filter (MilliporeSigma™ Amicon™) and then centrifuged in a Sorvall MTX 150 Micro-Ultracentrifuge (Thermo Fisher Scientific) using a S100AT4 rotor for 30 min at 66,000 × *g* and 4 °C before injecting it into a size-exclusion chromatography (SEC) column. The protein was purified using a Superose™ 6 10/300 GL SEC column attached to an AKTA FPLC (GE Healthcare) and equilibrated with the buffer containing 150 mM NaCl, 20 mM Tris pH 8.0, 1 mM βME, and 0.01% (w/v) GDN. The tetrameric peak fractions were pooled and concentrated using a 100-kDa NMWL centrifugal filter (MilliporeSigma™ Amicon™) to 3 mg/mL. MSP20 was added to hTRPV1 at the concentration of 200 μM.

Cryo-EM sample preparation and data collection

UltrAuFoil 1.2/1.3, Au-50 (300-mesh) grids were used for plunge-freezing. Prior to sample application, grids were plasma treated in a

PELCO easiGlow glow discharge cleaning system (0.39 mBar, 15 mA, "glow" for 25 s, and "hold" for 10 s). A Mark IV Vitrobot (Thermo Fisher Scientific) set to 100% humidity at 4 °C was used to plunge-freeze the grids in liquid ethane after applying 3 μL of protein sample to their gold-coated side using a blot time of 5 s, a blot force of 5, and a wait time of 15 s. The grids were stored in liquid nitrogen before imaging. Images of frozen-hydrated particles of $hTRPV1_{MSP20}$ were collected on a Titan Krios transmission electron microscope (Thermo Fisher Scientific) operating at 300 kV and equipped with a post-column GIF Quantum energy filter and a Gatan K3 Summit direct electron detection camera (Gatan, Pleasanton, CA, USA). 12,312 micrographs were collected in counting mode with raw image pixel size of 0.856 Å across the defocus range of −0.6 to −1.6 μm. The total dose of ~60 $e^{-}Å^{-2}$ was attained by using the dose rate of ~16.29 $e^{-}pixel^{-1}s^{-1}$ across 50 frames during the 2.7-s exposure time.

Image processing and 3D reconstruction

Data were processed in cryoSPARC 4.4[80], processing workflow is presented in Supplementary Fig. 7. Movie frames were aligned using the patch motion correction in cryoSPARC. Contrast transfer function (CTF) estimation was performed on non-dose-weighted micrographs using the patch CTF estimation. Subsequent data processing was done on dose-weighted micrographs. Following CTF estimation, micrographs were manually inspected and those with lower predicted CTF-correlated resolution (higher than 6 Å) were excluded from further processing. After several rounds of selection through 2D classification, particles were further 3D classified (heterogeneous refinement) into four classes. Particles representing the best class were re-extracted without binning (256-pixel box size) and further 3D classified; the best subset of particles was used for training Topaz model[81] followed by 2D- and 3D-classification cleanup. Obtained set of 250,351 particles representing the best class was subjected to homogenous refinement without symmetry and followed by non-uniform refinement[82] with simultaneous global and local CTF refinement using C4 symmetry. Reference-based motion correction was performed on the aligned particles with subsequent non-uniform refinement using previous parameters. Final round of 3D classification with 10 classes yielded one predominant class, containing 249,242 particles. The subset of particles was used for the final non-uniform refinement with C4 symmetry enforced resulting in 2.68 Å reconstruction. The reported resolution of 2.60 Å for the final map of $hTRPV1_{MSP20}$ was estimated using the gold standard Fourier Shell Correlation (FSC) after rescaling the obtained map on EMD-29983 in ChimeraX[83]. The rescaling of the map was done as a correction of imprecise calibration of magnified pixel size and EMD-29983 was chosen as the highest resolution cryo-EM reconstruction of human TRPV1. The local resolution was calculated with the resolution range estimated using the FSC = 0.143 criterion in cryoSPARC 4.4. Cryo-EM density visualization was done in UCSF Chimera[84] and UCSF ChimeraX[83].

Model building

To build the model of $hTRPV1_{MSP20}$ in Coot[85], we used the previously published apo-state cryo-EM structure of hTRPV1 ($hTRPV1_{Apo}$; PDB ID: 8GF8) as a guide. The model was tested for overfitting by shifting its coordinates by 0.5 Å (using Shake) in Phenix[86], refining the shaken model against the corresponding unfiltered half map, and generating densities from the resulting model in UCSF Chimera. Structures were visualized and figures were prepared in UCSF Chimera, UCSF ChimeraX[83], and Pymol[87]. The pore radius was calculated using HOLE[88].

Whole-cell patch-clamp recordings

Genes encoding human TRPV1 (wild type, Y511A, S512A, R557K, R557A, and A666W) were cloned into a pIRES expression vector, enabling bicistronic expression together with green fluorescent protein via a downstream internal ribosome entry site[89]. HEK293 cells (ATCC CRL-1573), cultured in 24-well plates, were transiently transfected with 200–500 ng plasmid DNA using Lipofectamine 2000 (Invitrogen) according to the manufacturer's instructions. Cells were transferred onto glass coverslips, and recordings were performed 20–48 h after transfection at RT.

Whole-cell currents were recorded at a holding potential of −60 mV using an Axopatch 200B amplifier (Molecular Devices), low-pass filtered at 5 kHz, and digitized at 10 kHz with a Digidata 1550B data acquisition system and pCLAMP 11.4 software (Molecular Devices). Patch pipettes had resistances of 2–6 MΩ. The extracellular solution contained (in mM): 140 NaCl, 5 KCl, 2 $MgCl_2$, 10 glucose, and 10 HEPES (pH 7.4). The intracellular (pipette) solution contained (in mM): 150 KCl, 3 $MgCl_2$, 5 EGTA, and 10 HEPES (pH 7.2).

MSP20 was applied at the indicated concentrations via the extracellular solution. Rapid solution exchange was achieved using a two-barrel theta-glass pipette mounted on a piezoelectric translator. For most experiments, agonist was applied for 5 s, followed by a 2-min interval between applications to allow completion of slow, non-electrogenic kinetic steps in TRPV1 and to permit switching to the next agonist concentration. Desensitization at high MSP20 concentration was examined using a prolonged 20-s agonist application. Data analysis was performed using in-house–written Python scripts.

Molecular dynamic simulations details

The Orientations of Proteins in Membranes (OPM) database[90] was utilized to align the obtained $TRPV1_{MSP20}$ channel along the Z-axis, embedding it within a POPC (1-palmitoyl-2-oleoyl-sn-glycerol-3-phosphocholine) lipid bilayer. The system was then solvated in an orthorhombic box containing single-point charge (SPC) water molecules, and chloride ions were added to ensure electroneutrality (Supplementary Table 7). Molecular dynamics (MD) simulations were conducted using Desmond[91], as implemented in the Maestro/Schrödinger suite, with the OPLS_2005 force field applied. Each system was first subjected to the standard Desmond relaxation protocol to gradually equilibrate the system before production MD. Initially, the system underwent energy minimization to remove steric clashes and relax the starting geometry, with positional restraints applied to the heavy atoms of the solute. This was followed by a short MD run at low temperature (10 K) in the NVT ensemble, maintaining restraints on the solute heavy atoms to allow the solvent to relax around the solute. The restraints were then progressively reduced through a series of short MD simulations in the NPT ensemble at the target temperature (300 K). These steps included simulations with restraints on all solute atoms, followed by only the backbone, and finally unrestrained simulations. Finally, a fully unrestrained NPT simulation was performed to ensure the system reached stable thermodynamic conditions, with temperature, pressure, and density equilibrated prior to the production runs. NPT ensemble conditions were applied, maintaining a temperature of 300 K via the Nosé–Hoover chain thermostat and a pressure of 1 atm using the Martyna–Tobias–Klein barostat. The short-range cutoff method with a cutoff radius of 9.0 Å was used to calculate Coulombic interactions. Bonded interactions were integrated using the RESPA algorithm at 2.0 fs timestep. For each equilibrated system, three independent production runs of 200 ns each were carried out. For the purpose of analysing ligand–receptor interactions, including hydrogen bonds, π–π stacking, hydrophobic contacts, and distances between key residues, 200 ns of production MD per replicate are sufficient. These events occur on a relatively fast timescale and stabilize quickly once the system is equilibrated. Furthermore, performing three independent replicas ensures adequate statistical sampling of the interactions, making enhanced sampling methods unnecessary for the scope of this study. This approach ensures comprehensive exploration of the conformational landscape around the experimental starting structure and minimizes dependence on the initial configuration. To compare the dynamic behaviour of hTRPV1 in complex with MSP20, we analysed it

relative to the RTx-bound open state model (PDB ID: 7RQW)[53], for which three independent production runs of 200 ns each were also performed. For each replica, the mean and standard deviation were calculated for each system to analyse the dynamics. Relevant data, including interactions such as H-bonds and salt bridges, distances between residues, and SASA, were extracted from the simulation trajectories using the internal tools available in Desmond. The SASA was calculated for each residue at the interface of all four chains forming the pore, allowing us to assess changes in solvent exposure during the simulation. A MD checklist for data reproducibility is provided as a Supplementary Table 8. The initial and final coordinates of both $hTRPV1_{MSP20}$ and $rTRPV1_{open}$ complexes extrapolated from the first and the last frame, respectively, of the MDs three replicates are reported in Supplementary Data 1–12. To assess the state of the TRPV1 channel pore and quantify its conductance (Gmacro), expressed in pS, during the 200 ns of MD simulations, we used the HOLE[88] program for 1000 snapshots of both RTx-bound and MSP20-bound structures. Figures were prepared in UCSF Chimera and VMD software[92].

Reporting summary

Further information on research design is available in the Nature Portfolio Reporting Summary linked to this article.

Data availability

All data needed to evaluate the conclusions of the paper are present in the paper or the Supplementary Information. ^{1}H-and ^{13}C-NMR spectra, UPLC-MS/HPLC-MS and HRMS traces of amides **2**–**9** (see Supplementary pages 5-66). Theoretical binding free energy values and ADME parameters of the selected top three hits (see Supplementary Table 1). Superposition of binding mode of capsaicin, **2a** and **3a** compounds in the TRPV1 vanilloid-binding site (see Supplementary Fig. 1). Activating (EC_{50}) and inhibitory/desensitizing (IC_{50}) potency of MSP20 for TRPV3, TRPV4 and TRPM8 (see Supplementary Table 2). Fluorescence plots of MSP20 (see Supplementary Fig. 2). Cell viability and cytotoxicity assays (see Supplementary Fig. 3). In vitro absorption, distribution, metabolism, and excretion studies of MSP20 (see Supplementary Table 3). Possible metabolite formed after aromatic oxidation (see Supplementary Fig. 4). Results of the antioxidant (ABTS and DPPH) activity of Trolox, Capsaicin, and MSP20 (see Supplementary Table 4). Effect of MSP20 on rat brain slice viability in the model of glutamate-induced excitotoxicity (see Supplementary Fig. 5). Effect of MSP20 on body temperature in mice (see Supplementary Fig. 6). Workflow of cryo-EM data processing (see Supplementary Fig. 7). Overview of cryo-EM data for $hTRPV1_{MSP20}$ (see Supplementary Fig. 8). Examples of cryo-EM density (see Supplementary Fig. 9). Time evolution of H-bonds and salt-bridges between D576 and R579, and H-bonds between N560 and Q561 over 100 ns of molecular dynamics simulations of rep1 (see Supplementary Fig. 10). Experimental conditions for chromatographic separation for ADME studies (see Supplementary Table 5). Experimental protocol used to assess the neuroprotective effects (see Supplementary Fig. 11). Molecular dynamic simulations details (see Supplementary Table 7). MD checklist for data reproducibility (see Supplementary Table 8). The cryo-EM density map of hTRPV1 in complex with MSP20 was deposited to the Electron Microscopy Data Bank (EMDB) under the accession code EMD-71555 ($hTRPV1_{MSP20}$ [https://www.ebi.ac.uk/pdbe/entry/emdb/EMD-71555]). The atomic coordinates have been deposited to the Protein Data Bank (PDB) under the accession code 9PEA ($hTRPV1_{MSP20}$ [https://doi.org/10.2210/pdb9PEA/pdb]) (see Supplementary Table 6). Source data are provided with this paper.

References

1. Gladkikh, I. N., Sintsova, O. V., Leychenko, E. V. & Kozlov, S. A. TRPV1 ion channel: structural features, activity modulators, and therapeutic potential. *Biochemistry* **86**, 50–70 (2021).
2. Baskaran, P. et al. TRPV1 activation counters diet-induced obesity through sirtuin-1 activation and PRDM-16 deacetylation in brown adipose tissue. *Int. J. Obes.* **41**, 739–749 (2017).
3. Ji, R.-R., Nackley, A., Huh, Y., Terrando, N. & Maixner, W. Neuroinflammation and central sensitization in chronic and widespread pain. *Anesthesiology* **129**, 343–366 (2018).
4. Szallasi, A. & Blumberg, P. M. Vanilloid (capsaicin) receptors and mechanisms. *Pharmacol. Rev.* **51**, 159–212 (1999).
5. Jancso, G., Oszlacs, O. & Santha, P. The capsaicin paradox: pain relief by an algesic agent. *Antiinflamm. Antiallergy Agents Med. Chem.* **10**, 52–65 (2011).
6. Arora, V., Campbell, J. N. & Chung, M.-K. Fight fire with fire: neurobiology of capsaicin-induced analgesia for chronic pain. *Pharmacol. Ther.* **220**, 107743 (2021).
7. Iftinca, M., Defaye, M. & Altier, C. TRPV1-targeted drugs in development for human pain conditions. *Drugs* **81**, 7–27 (2021).
8. Abdel-Salam, O. M. E. & Mózsik, G. Capsaicin, the vanilloid receptor TRPV1 agonist in neuroprotection: mechanisms Involved and Significance. *Neurochem. Res.* **48**, 3296–3315 (2023).
9. Luo, X.-J., Peng, J. & Li, Y.-J. Recent advances in the study on capsaicinoids and capsinoids. *Eur. J. Pharmacol.* **650**, 1–7 (2011).
10. Romeo, I. et al. In silico-guided rational drug design and synthesis of novel 4-(thiophen-2-yl)butanamides as potent and selective TRPV1 agonists. *J. Med. Chem.* **66**, 6994–7015 (2023).
11. Caballero, J. A new era for the design of TRPV1 antagonists and agonists with the use of structural information and molecular docking of capsaicin-like compounds. *J. Enzym. Inhib. Med. Chem.* **37**, 2169–2178 (2022).
12. Aiello, F. et al. Design and synthesis of new transient receptor potential vanilloid type-1 (TRPV1) channel modulators: identification, molecular modeling analysis, and pharmacological characterization of the *N* -(4-hydroxy-3-methoxybenzyl)-4-(thiophen-2-yl)butanamide, a small molecule endowed with agonist TRPV1 activity and protective effects against oxidative stress. *ACS Chem. Neurosci.* **7**, 737–748 (2016).
13. Genheden, S. & Ryde, U. The MM/PBSA and MM/GBSA methods to estimate ligand-binding affinities. *Expert Opin. Drug Discov.* **10**, 449–461 (2015).
14. Yelshanskaya, M. V. & Sobolevsky, A. I. Ligand-binding sites in vanilloid-subtype TRP channels. *Front Pharm.* **13**, 900623 (2022).
15. Talyzina, I. A., Nadezhdin, K. D. & Sobolevsky, A. I. Forty sites of TRP channel regulation. *Curr. Opin. Chem. Biol.* **84**, 102550 (2025).
16. Neuberger, A. et al. Human TRPV1 structure and inhibition by the analgesic SB-366791. *Nat. Commun.* **14**, 2451 (2023).
17. Ajay, Bemis, G. W. & Murcko, M. A. Designing libraries with CNS activity. *J. Med. Chem.* **42**, 4942–4951 (1999).
18. Ghose, A. K., Herbertz, T., Hudkins, R. L., Dorsey, B. D. & Mallamo, J. P. Knowledge-based, central nervous system (CNS) lead selection and lead optimization for CNS drug discovery. *ACS Chem. Neurosci.* **3**, 50–68 (2012).
19. Brizzi, A. et al. Structure–affinity relationships and pharmacological characterization of new alkyl-resorcinol cannabinoid receptor ligands: Identification of a dual cannabinoid receptor/TRPA1 channel agonist. *Bioorg. Med. Chem.* **22**, 4770–4783 (2014).
20. Kritis, A. A., Stamoula, E. G., Paniskaki, K. A. & Vavilis, T. D. Researching glutamate-induced cytotoxicity in different cell lines: a comparative/collective analysis/study. *Front. Cell. Neurosci.* **9**, 91 (2015).
21. Santulli, C. et al. Castanea sativa Mill. Bark extract protects U-373 MG cells and rat brain slices against ischemia and reperfusion injury. *J. Cell. Biochem.* **118**, 839–850 (2017).
22. Liao, R., Wood, T. R. & Nance, E. Superoxide dismutase reduces monosodium glutamate-induced injury in an organotypic whole hemisphere brain slice model of excitotoxicity. *J. Biol. Eng.* **14**, 3 (2020).

23. Molz, S. et al. Glutamate-induced toxicity in hippocampal slices involves apoptotic features and p38MAPK signaling. *Neurochem. Res.* **33**, 27–36 (2008).
24. Alex, A. B., Saunders, G. W., Dalpé-Charron, A., Reilly, C. A. & Wilcox, K. S. CGX-1007 prevents excitotoxic cell death via actions at multiple types of NMDA receptors. *Neurotoxicology* **32**, 392–399 (2011).
25. Zou, J. Y. & Crews, F. T. TNFα potentiates glutamate neurotoxicity by inhibiting glutamate uptake in organotypic brain slice cultures: neuroprotection by NFκB inhibition. *Brain. Res.* **1034**, 11–24 (2005).
26. Fan, G., Liu, M., Liu, J. & Huang, Y. The initiator of neuroexcitotoxicity and ferroptosis in ischemic stroke: glutamate accumulation. *Front. Mol. Neurosci.* **16**, 1113081 (2023).
27. Wu, W., Gong, X., Qin, Z. & Wang, Y. Molecular mechanisms of excitotoxicity and their relevance to the pathogenesis of neurodegenerative diseases—an update. *Acta Pharmacol. Sin.* **46**, 3129–3142 (2025).
28. Gruenbaum, B. F., Zlotnik, A., Fleidervish, I., Frenkel, A. & Boyko, M. Glutamate neurotoxicity and destruction of the blood–brain barrier: key pathways for the development of neuropsychiatric consequences of TBI and their potential treatment strategies. *Int. J. Mol. Sci.* **23**, 9628 (2022).
29. Chen, J. et al. Protective effects of Δ9-tetrahydrocannabinol against *N*-methyl-D-aspartate-induced AF5 cell death. *Mol. Brain Res.* **134**, 215–225 (2005).
30. Chen, L. et al. Capsaicin attenuates amyloid-β-induced synapse loss and cognitive impairments in mice. *J. Alzheimer Dis.* **59**, 683–694 (2017).
31. Chen, C. et al. Signal transduction for inhibition of inducible nitric oxide synthase and cyclooxygenase-2 induction by capsaicin and related analogs in macrophages. *Br. J. Pharmacol.* **140**, 1077–1087 (2003).
32. Henderson, D. E., Slickman, A. M. & Henderson, S. K. Quantitative HPLC determination of the antioxidant activity of capsaicin on the formation of lipid hydroperoxides of linoleic acid: a comparative study against BHT and melatonin. *J. Agric. Food Chem.* **47**, 2563–2570 (1999).
33. Kogure, K. Mechanism of potent antiperoxidative effect of capsaicin. *BBA Gen. Subj.* **1573**, 84–92 (2002).
34. Ochi, T., Takaishi, Y., Kogure, K. & Yamauti, I. Antioxidant activity of a new capsaicin derivative from capsicum annuum. *J. Nat. Prod.* **66**, 1094–1096 (2003).
35. Coderre, T. & Melzack, R. The contribution of excitatory amino acids to central sensitization and persistent nociception after formalin-induced tissue injury. *J. Neurosci.* **12**, 3665–3670 (1992).
36. Tjølsen, A., Berge, O.-G., Hunskaar, S., Rosland, J. H. & Hole, K. The formalin test: an evaluation of the method. *Pain* **51**, 5–17 (1992).
37. Marini, E., Magi, G., Mingoia, M., Pugnaloni, A. & Facinelli, B. Antimicrobial and anti-virulence activity of capsaicin against erythromycin-resistant, cell-invasive group A streptococci. *Front. Microbiol.* **6**, 01281 (2015).
38. Kirkedal, C., Wegener, G., Moreira, F., Joca, S. R. L. & Liebenberg, N. A dual inhibitor of FAAH and TRPV1 channels shows dose-dependent effect on depression-like behaviour in rats. *Acta Neuropsychiatr.* **29**, 324–329 (2017).
39. Linares, I. M. et al. Cannabidiol presents an inverted U-shaped dose-response curve in a simulated public speaking test. *Braz. J. Psychiatry* **41**, 9–14 (2019).
40. Haemmerle, G. et al. Defective lipolysis and altered energy metabolism in mice lacking adipose triglyceride lipase. *Science* **312**, 734–737 (2006).
41. Decosterd, I. & Woolf, C. J. Spared nerve injury: an animal model of persistent peripheral neuropathic pain. *Pain* **87**, 149–158 (2000).
42. Nadezhdin, K. D. et al. Extracellular cap domain is an essential component of the TRPV1 gating mechanism. *Nat. Commun.* **12**, 2154 (2021).
43. Cao, E., Liao, M., Cheng, Y. & Julius, D. TRPV1 structures in distinct conformations reveal activation mechanisms. *Nature* **504**, 113–118 (2013).
44. Gao, Y., Cao, E., Julius, D. & Cheng, Y. TRPV1 structures in nanodiscs reveal mechanisms of ligand and lipid action. *Nature* **534**, 347–351 (2016).
45. Liao, M., Cao, E., Julius, D. & Cheng, Y. Structure of the TRPV1 ion channel determined by electron cryo-microscopy. *Nature* **504**, 107–112 (2013).
46. Zhang, F. et al. Heat activation is intrinsic to the pore domain of TRPV1. *Proc. Natl. Acad. Sci.* **115**, E317–E324 (2018).
47. Tominaga, M. et al. The cloned capsaicin receptor integrates multiple pain-producing stimuli. *Neuron* **21**, 531–543 (1998).
48. Nadezhdin, K. D. et al. TRPV3 activation by different agonists accompanied by lipid dissociation from the vanilloid site. *Sci. Adv.* **10**, eadn2453 (2024).
49. Welch, J. M., Simon, S. A. & Reinhart, P. H. The activation mechanism of rat vanilloid receptor 1 by capsaicin involves the pore domain and differs from the activation by either acid or heat. *Proc. Natl. Acad. Sci.* **97**, 13889–13894 (2000).
50. Caterina, M. J. et al. The capsaicin receptor: a heat-activated ion channel in the pain pathway. *Nature* **389**, 816–824 (1997).
51. Ohbuchi, K. et al. Detailed analysis of the binding mode of vanilloids to transient receptor potential vanilloid type I (TRPV1) by a mutational and computational study. *PLoS ONE* **11**, e0162543 (2016).
52. Nadezhdin, K. D. et al. Structure of human TRPV4 in complex with GTPase RhoA. *Nat. Commun.* **14**, 3733 (2023).
53. Kwon, D. H., Zhang, F., Fedor, J. G., Suo, Y. & Lee, S.-Y. Vanilloid-dependent TRPV1 opening trajectory from cryoEM ensemble analysis. *Nat. Commun.* **13**, 2874 (2022).
54. Bonica, J. J. History of pain concepts and pain therapy. *Mt. Sinai J. Med.* **58**, 191–202 (1991).
55. Højsted, J. & Sjøgren, P. Addiction to opioids in chronic pain patients: a literature review. *Eur. J. Pain.* **11**, 490–518 (2007).
56. Julius, D. TRP channels and pain. *Annu. Rev. Cell Dev. Biol.* **29**, 355–384 (2013).
57. Marrone, M. C. et al. TRPV1 channels are critical brain inflammation detectors and neuropathic pain biomarkers in mice. *Nat. Commun.* **8**, 15292 (2017).
58. Niiyama, Y., Kawamata, T., Yamamoto, J., Omote, K. & Namiki, A. Bone cancer increases transient receptor potential vanilloid subfamily 1 expression within distinct subpopulations of dorsal root ganglion neurons. *Neuroscience* **148**, 560–572 (2007).
59. Iglesias, L. P., Aguiar, D. C. & Moreira, F. A. TRPV1 blockers as potential new treatments for psychiatric disorders. *Behav. Pharmacol.* **33**, 2–14 (2022).
60. Aghazadeh Tabrizi, M. et al. Medicinal chemistry, pharmacology, and clinical implications of TRPV1 receptor antagonists. *Med. Res. Rev.* **37**, 936–983 (2017).
61. Casarotto, P. C. et al. Opposing roles for cannabinoid receptor type-1 (CB 1) and transient receptor potential vanilloid Type-1 channel (TRPV1) on the modulation of panic-like responses in rats. *Neuropsychopharmacology* **37**, 478–486 (2012).
62. Fogaça, M. V., Aguiar, D. C., Moreira, F. A. & Guimarães, F. S. The endocannabinoid and endovanilloid systems interact in the rat prelimbic medial prefrontal cortex to control anxiety-like behavior. *Neuropharmacology* **63**, 202–210 (2012).
63. Marsch, R. et al. Reduced anxiety, conditioned fear, and hippocampal long-term potentiation in transient receptor potential vanilloid type 1 receptor-deficient mice. *J. Neurosci.* **27**, 832–839 (2007).

64. Papa, A. et al. Corrigendum: Long-term efficacy and reduced side-effects of buprenorphine in patients with moderate and severe chronic pain. *Front. Pharmacol.* **15**, 1491886 (2024).
65. Jorgensen, W. L., Maxwell, D. S. & Tirado-Rives, J. Development and testing of the OPLS all-atom force field on conformational energetics and properties of organic liquids. *J. Am. Chem. Soc.* **118**, 11225–11236 (1996).
66. Friesner, R. A. et al. Glide: a new approach for rapid, accurate docking and scoring. 1. Method and assessment of docking accuracy. *J. Med. Chem.* **47**, 1739–1749 (2004).
67. Moriello, A. S., De Petrocellis, L. & Vitale, R. M. Fluorescence-based assay for TRPV1 channels. *Methods Mol. Biol.* **2576**, 119–131 (2023).
68. Mazzotta, S. et al. Pinocembrin and its linolenoyl ester derivative induce wound healing activity in HaCaT cell line potentially involving a GPR120/FFA4 mediated pathway. *Bioorg. Chem.* **108**, 104657 (2021).
69. Poggialini, F. et al. Biological evaluation and in vitro characterization of ADME profile of in-house pyrazolo[3,4-d]pyrimidines as dual tyrosine kinase inhibitors active against glioblastoma multiforme. *Pharmaceutics* **15**, 453 (2023).
70. Molinari, A. et al. Efficient optimization of pyrazolo[3,4-d]pyrimidines derivatives as c-Src kinase inhibitors in neuroblastoma treatment. *Bioorg. Med. Chem. Lett.* **28**, 3454–3457 (2018).
71. Poggialini, F. et al. Sweet cherry extract as permeation enhancer of tyrosine kinase inhibitors: a promising prospective for future oral anticancer therapies. *Pharmaceuticals* **16**, 1527 (2023).
72. Chiaino, E. et al. Acacia catechu willd. Extract protects neuronal cells from oxidative stress-induced damage. *Antioxidants* **11**, 81 (2021).
73. Chiaino, E. et al. Olive leaves and hibiscus flowers extracts-based preparation protect brain from oxidative stress-induced injury. *Antioxidants* **9**, 806 (2020).
74. Ann, J. et al. Discovery of nonpungent transient receptor potential vanilloid 1 (TRPV1) agonist as strong topical analgesic. *J. Med. Chem.* **63**, 418–424 (2020).
75. Meunier, A. et al. Attenuation of pain-related behavior in a rat model of trigeminal neuropathic pain by viral-driven enkephalin overproduction in trigeminal ganglion neurons. *Mol. Ther.* **11**, 608–616 (2005).
76. Neuberger, A., Nadezhdin, K. D. & Sobolevsky, A. I. TRPV3 expression and purification for structure determination by Cryo-EM. *Methods Enzymol.* **652**, 31–48 (2021).
77. Neuberger, A., Nadezhdin, K. D. & Sobolevsky, A. I. Structural mechanism of TRPV3 channel inhibition by the anesthetic dyclonine. *Nat. Commun.* **13**, 2795 (2022).
78. Neuberger, A., Nadezhdin, K. D., Zakharian, E. & Sobolevsky, A. I. Structural mechanism of TRPV3 channel inhibition by the plant-derived coumarin osthole. *EMBO Rep.* **22**, e53233 (2021).
79. Goehring, A. et al. Screening and large-scale expression of membrane proteins in mammalian cells for structural studies. *Nat. Protoc.* **9**, 2574–2585 (2014).
80. Punjani, A., Rubinstein, J. L., Fleet, D. J. & Brubaker, M. A. cryoSPARC: algorithms for rapid unsupervised cryo-EM structure determination. *Nat. Methods* **14**, 290–296 (2017).
81. Bepler, T. et al. Positive-unlabeled convolutional neural networks for particle picking in cryo-electron micrographs. *Nat. Methods* **16**, 1153–1160 (2019).
82. Punjani, A., Zhang, H. & Fleet, D. J. Non-uniform refinement: adaptive regularization improves single-particle cryo-EM reconstruction. *Nat. Methods* **17**, 1214–1221 (2020).
83. Pettersen, E. F. et al. UCSF ChimeraX: Structure visualization for researchers, educators, and developers. *Protein Sci.* **30**, 70–82 (2021).
84. Pettersen, E. F. et al. UCSF chimera—a visualization system for exploratory research and analysis. *J. Comput. Chem.* **25**, 1605–1612 (2004).
85. Emsley, P., Lohkamp, B., Scott, W. G. & Cowtan, K. Features and development of *Coot*. *Acta Crystallogr. D. Biol. Crystallogr.* **66**, 486–501 (2010).
86. Afonine, P. V. et al. Towards automated crystallographic structure refinement with *phenix.refine*. *Acta Crystallogr. D. Biol. Crystallogr.* **68**, 352–367 (2012).
87. *The PyMOL Molecular Graphics System* (DeLano Scientific, San Carlos, CA, USA, 2002).
88. Smart, O. S., Neduvelil, J. G., Wang, X., Wallace, B. A. & Sansom, M. S. P. HOLE: a program for the analysis of the pore dimensions of ion channel structural models. *J. Mol. Graph.* **14**, 354–360 (1996).
89. Yelshanskaya, M. V., Li, M. & Sobolevsky, A. I. Structure of an agonist-bound ionotropic glutamate receptor. *Science* **345**, 1070–1074 (2014).
90. Søndergaard, C. R., Olsson, M. H. M., Rostkowski, M. & Jensen, J. H. Improved treatment of ligands and coupling effects in empirical calculation and rationalization of p *K* a values. *J. Chem. Theory Comput.* **7**, 2284–2295 (2011).
91. Bowers, K. J. et al. Scalable algorithms for molecular dynamics simulations on commodity clusters. *Proceedings of the 2006 ACM/IEEE Conference on Supercomputing (SC-06)* **SC-06**, 43–43 (2006).
92. Humphrey, W., Dalke, A. & Schulten, K. VMD: visual molecular dynamics. *J. Mol. Graph.* **14**, 33–38 (1996).

Acknowledgements

We thank Dr. Simone Esposito from Dipartimento di DMPK, IRBM, Pomezia (Rome), Italy, for UPLC-MS determinations, and Professor M. Taddei for granting the use of the 600 MHz NMR instrument. We thank Robert Grassucci and Zhening Zhang (Columbia University Cryo-Electron Microscopy Center) for help with microscope operation and data collection. Some of this work was performed at the Columbia University Cryo-Electron Microscopy Center.

Author contributions

A.N. carried out protein expression, protein purification, and prepared cryo-EM samples. A.N. and I.A.T. performed cryo-EM data processing. A.N., I.A.T. and A.I.S. analysed structural data and built molecular models. A.A. performed electrophysiological patch-clamp experiments and analysed their results. A.B., F.A., I.R. and S.Maramai carried out the design, synthesis and characterization of the compounds. I.R. performed the molecular modelling calculations and analysed the data. L.D.P. and A.S.M. carried out fluorescent measurements of intracellular calcium concentration. M.F. and F.P. conceived, planned, carried out and analysed the in vitro experiments on cells and brain slices. L.L. and S.M. designed and planned the in vivo experiments on mice. C.B., A.M.M., M.P. and R.B. conducted the in vivo experiments. C.V. and F.P. developed the methodology and carried out the formal analysis of ADME experiments as well as the DPPH and ABTS assays. E.D. supervised ADME experiments. A.N., I.A.T., A.I.S., I.R., A.A., S.A., S.Maramai, A.B. and F.A. wrote the original draft of the manuscript. All authors contributed to the writing and editing of this manuscript. All authors have given approval to the final version of the manuscript.

Funding

This research was, in part, supported by the National Cancer Institute's National Cryo-EM Facility at the Frederick National Laboratory for Cancer Research under contract 75N91019D00024. A portion of this research was supported by NIH grant U24GM129547 and performed at the PNCC at OHSU and accessed through EMSL (grid.436923.9), a DOE Office of Science User Facility sponsored by the Office of Biological and Environmental Research. A.N. was a Walter Benjamin Fellow funded by the Deutsche Forschungsgemeinschaft (DFG, German Research

Foundation)-464295817. A.I.S. was supported by the Human Frontier Science Program (HFSP) Award and the NIH (CA206573). This research was supported by "Piano Sostegno alla Ricerca", Dipartimento di Biotecnologie, Chimica e Farmacia (Università di Siena) and Dipartimento di Farmacia e Scienze della Salute e della Nutrizione, Università della Calabria). M.F. was supported by UNISI (2264-2023-FM-PSR-RUNNERSUP_002). I.R., A.A. and S.A. were supported by the MUR PRIN research project 201744BN5T.

Competing interests
The authors declare no competing interests.

Additional information
Supplementary information The online version contains supplementary material available at https://doi.org/10.1038/s41467-026-74972-3.

Correspondence and requests for materials should be addressed to Samuele Maramai, Stefano Alcaro or Alexander I. Sobolevsky.

Peer review information *Nature Communications* thanks Abdelrahim Alqudah, Sushant Kumar, Fan Yang, and the other, anonymous, reviewers for their contribution to the peer review of this work. A peer review file is available.

Reprints and permissions information is available at http://www.nature.com/reprints

Publisher's note Springer Nature remains neutral with regard to jurisdictional claims in published maps and institutional affiliations.

Open Access This article is licensed under a Creative Commons Attribution-NonCommercial-NoDerivatives 4.0 International License, which permits any non-commercial use, sharing, distribution and reproduction in any medium or format, as long as you give appropriate credit to the original author(s) and the source, provide a link to the Creative Commons licence, and indicate if you modified the licensed material. You do not have permission under this licence to share adapted material derived from this article or parts of it. The images or other third party material in this article are included in the article's Creative Commons licence, unless indicated otherwise in a credit line to the material. If material is not included in the article's Creative Commons licence and your intended use is not permitted by statutory regulation or exceeds the permitted use, you will need to obtain permission directly from the copyright holder. To view a copy of this licence, visit http://creativecommons.org/licenses/by-nc-nd/4.0/.

© The Author(s) 2026

[1]Department of Biochemistry and Molecular Biophysics, Columbia University, New York, NY, USA. [2]Dipartimento di Scienze della Salute, Università degli Studi "Magna Græcia" di Catanzaro, Campus "S. Venuta", Viale Europa, Catanzaro, Italy. [3]Net4Science Academic Spin-Off, Università degli Studi "Magna Græcia" di Catanzaro, Campus "S. Venuta", Viale Europa, Catanzaro, Italy. [4]Dipartimento di Farmacia e Scienza della Salute e della Nutrizione, Università della Calabria, Via P. Bucci, Cosenza, Italy. [5]Dipartimento di Biotecnologie, Chimica e Farmacia, Università di Siena, Siena, Italy. [6]Dipartimento di Medicina Molecolare e dello Sviluppo, Università di Siena, Siena, Italy. [7]Dipartimento di Scienze della Vita, Università di Siena, Siena, Italy. [8]Endocannabinoid Research Group, Istituto di Chimica Biomolecolare, Consiglio Nazionale delle Ricerche, Pozzuoli, Italy. [9]Epitech Group SpA, Saccolongo, Italy. [10]Dipartimento di Medicina Sperimentale, Divisione di Farmacologia, Università degli Studi della Campania "L. Vanvitelli", Napoli, Italy. [11]Integrated Program in Cellular, Molecular and Biomedical Studies, Columbia University, New York, NY, USA. [12]These authors contributed equally: Arthur Neuberger, Isabella Romeo, Francesca Aiello, Alexey Alekseev. [13]These authors jointly supervised this work: Anna Artese, Antonella Brizzi, Alexander I. Sobolevsky. ✉e-mail: samuele.maramai@unisi.it; alcaro@unicz.it; as4005@cumc.columbia.edu